Vortex molecular crystal and vortex plastic crystal states in honeycomb and kagomé pinning arrays

C. Reichhardt and C. J. Olson Reichhardt
Theoretical Division and Center for Nonlinear Studies, Los Alamos National Laboratory, Los Alamos, New Mexico 87545, USA
(Received 5 April 2007; revised manuscript received 5 July 2007; published 17 August 2007)

Using numerical simulations, we investigate vortex configurations and pinning in superconductors with honeycomb and kagomé pinning arrays. We find that a variety of vortex crystal states can be stabilized at integer and fractional matching field densities. The honeycomb and kagomé pinning arrays produce considerably more pronounced commensuration peaks in the critical depinning force than triangular pinning arrays, and also cause additional peaks at noninteger matching fields where a portion of the vortices are located in the large interstitial regions of the pinning lattices. For the honeycomb pinning array, we find matching effects of equal strength at most fillings $B/B_\phi=n/2$ for $n>2$, where n is an integer, in agreement with recent experiments. For kagomé pinning arrays, pronounced matching effects generally occur at $B/B_\phi=n/3$ for $n>3$, while for triangular pinning arrays pronounced matching effects are observed only at integer fillings $B/B_\phi=n$. At the noninteger matching field peaks in the honeycomb and kagomé pinning arrays, the interstitial vortices are arranged in dimer, trimer, and higher order n-mer states that have an overall orientational order. We call these n-mer states "vortex molecular crystals" and "vortex plastic crystals" since they are similar to the states recently observed in colloidal molecular crystal systems. We argue that the vortex molecular crystals have properties in common with certain spin systems such as Ising and n-state Potts models. We show that kagomé and honeycomb pinning arrays can be useful for increasing the critical current above that of purely triangular pinning arrays.

DOI: 10.1103/PhysRevB.76.064523 PACS number(s): 74.25.Qt

I. INTRODUCTION

There have been extensive studies on the static and dynamical properties of vortices in superconductors with periodic arrays of artificial pinning sites. These works focused on simple two-dimensional periodic pinning arrays such as square, triangular, and rectangular lattices, where the pinning sites consist of holes,[1–9] blind holes,[10,11] or magnetic dots.[12–18] For square and triangular pinning arrays, pronounced commensurability effects such as peaks or anomalies in the critical current appear at the magnetic field $B=B_\phi$, where the number of vortices equals the number of pinning sites, as well as at higher fields $B=nB_\phi$, where n is an integer. At these matching fields, the vortex lattice forms ordered crystalline structures of a type determined by the number of vortices that are captured at individual pinning sites. If more than one vortex can occupy each pinning site in the form of a multiquanta vortex, then at each matching field the overall vortex lattice has the same symmetry as the pinning lattice but is composed of n-quanta vortices. If only a single vortex can occupy each pinning site, ordered vortex crystals still form at the matching fields and for $n>1$ some of the vortices are located in the interstitial regions between the pinning sites. Imaging experiments[4] and simulations[7] for systems where at most one vortex can occupy each pin have shown that numerous kinds of interstitial vortex lattice structures can be stabilized, some of which have different symmetries than the pinning array. Interstitial vortex crystals also form above the pinning saturation field in samples with pins that can be occupied by multiquanta vortices. When each pin has captured as many vortices as possible, additional vortices sit in the interstitial regions, and the resulting vortex lattice structure is a composite of interstitial singly quantized and pinned multiply quantized vortices.[2,9,19,20] In the case where the pinning sites are blind holes, it is possible for multiple vortices to occupy a single pinning site without merging into a multiquanta vortex. Instead, the vortices retain their individual identities and form dimer, trimer, or ring-type states inside the pin.[10,21]

In addition to the matching effects that appear at integer fields, commensuration effects can also occur at nonmatching fields or fractional fields.[3,5,8,16] These noninteger matching effects are generally weaker than those observed at integer matching and are most prominent for fields $B<B_\phi$. If multiple vortex quantization occurs above the first matching field, the submatching sequence that appears between $B=0$ and $B=B_\phi$ is repeated between every integer matching field until the pinning sites are saturated. In contrast, if only one vortex is captured per pinning site, the fractional matching effects above the first matching field are significantly reduced or missing.[8] Commensuration effects for vortices interacting with a periodic substrate have also recently been demonstrated for vortices in Bose-Einstein condensates where the pinning sites are created with an optical array.[22–24]

The physics of vortices in periodic pinning arrays is similar to that of repulsively interacting colloids in triangular or square periodic trap arrays[25–29] and charged spheres on periodic substrates.[30] In both these cases, it is possible to have localized traps which capture only a single colloid or sphere while the remaining particles sit in the interstitial regions,[29,30] similar to the situation for vortex pinning arrays. The interstitial particles are more mobile than the pinned particles, and the particle trajectories resemble those seen in computer simulations of vortices in similar geometries.[31,32] In the colloid system, it is also possible for multiple colloids to be captured by a single trap[25–28] where they form dimer,

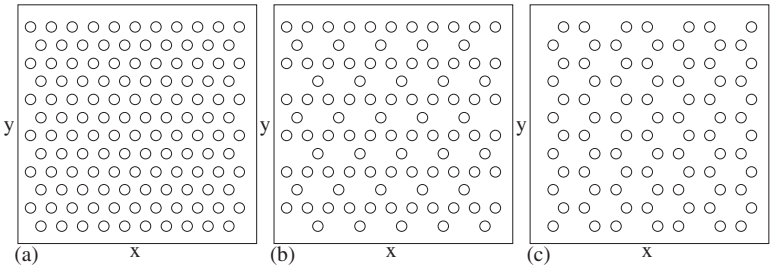

FIG. 1. The pinning site locations (circles) for periodic arrangements of sites forming (a) triangular, (b) kagomé, and (c) honeycomb arrays. Here, $B_\phi = 0.47\phi_0/\lambda^2$.

trimer, or higher order n-mer states. The n-mers may be orientationally ordered if the interaction between colloids in neighboring traps is strong enough, and the system can show multistage melting transitions in which the initial stage of melting occurs when the orientational ordering of the n-mers is lost, followed by a transition in which the n-mers break apart. The ordered n-mer states can be mapped onto various spin systems such as Ising and Potts models.[27,28] Orientationally ordered dimer and trimer states have also been proposed to occur for vortices in superconductors with blind hole arrays where the vortices retain single quantization in an individual hole.[8] The orientational ordering of the n-mer states in the colloidal and vortex systems arises due to quadrupole or higher order pole moment interactions between the n-mers in adjacent traps.[27] The anisotropic nature of the quadrupole and higher order pole moments creates preferred directions for the alignment of the n-mers that minimize the pole moment energy.

A limited number of studies have treated periodic substrates other than square and triangular pinning arrays, such as honeycomb or kagomé pinning arrays. These are simply triangular lattices with a fraction of the pinning sites removed. Figure 1(a) shows a triangular pinning lattice. Removing every other pinning site from every other row of the triangular lattice, which eliminates 1/4 of the pinning sites, produces the kagomé array illustrated in Fig. 1(b). A honeycomb array in which 1/3 of the pinning sites in the triangular array have been eliminated is shown in Fig. 1(c). Here, every third pinning site is removed from every row of the triangular array. An experimental study of pinning phenomena in kagomé arrays using superconductors with magnetic dot arrays produced evidence for pronounced commensurability effects at noninteger matching fields.[13] These results are, however, difficult to interpret since magnetic dot arrays can induce the formation of vortices or antivortices in addition to the vortices created by the external field.[17] Numerical work on kagomé pinning arrays[31] only treated thermal melting of vortices at a single field of $B/B_\phi = 2.0$, where a two step melting transition was shown to occur. Here, the multiple interstitial vortices located at the larger interstitial sites where a pin has been removed undergo local melting at a temperature below that at which the entire vortex lattice melts. In Ref. 31, neither long-range vortex configurations nor critical currents were analyzed, so the nature of commensurability effects for varied vortex densities in kagomé pinning arrays is not known.

Only a single experimental study[33] has been performed on honeycomb pinning arrays to our knowledge. In Ref. 33, several unusual features were observed, including pronounced matching effects of equal magnitude at magnetic fields corresponding to both integer and half-integer multiples of the matching field for vortex densities up to the fifth matching field $B/B_\phi = 5$. This result is in contrast to the response of square or triangular pinning arrays, where commensuration effects are much weaker at nonmatching fields than at integer matching fields. In Ref. 33, it was also observed that for fields greater than the second matching field, $B/B_\phi > 2$, the commensuration effects at half-integer matching fields become more prominent than those at integer matching fields. This effect can be understood by considering that since the honeycomb pinning array is simply a triangular pinning array that has been diluted by 1/3, the field $B/B_\phi = 1.5$ for the honeycomb array would correspond to an integer matching field $B/B_\phi = 1$ in a triangular array of the same density. As a result, the overall vortex lattice is triangular at $B/B_\phi = 1.5$ in a honeycomb pinning array. Similarly, a field of $B/B_\phi = 1/2$ in the honeycomb pinning array would correspond to a field of $B/B_\phi = 1/3$ in the equivalent triangular pinning array, which is known to produce a peak in the critical current.[8] These results suggest that honeycomb pinning arrays may allow for a variety of vortex structures to be stabilized at noninteger fillings.

In this work, we present an extensive study of vortex pinning and dynamics in honeycomb and kagomé pinning arrays using numerical simulations. Section II contains a description of the simulation method. We show the vortex configurations and ordering for honeycomb pinning arrays in Sec. III and illustrate the formation of vortex molecular crystals, which are named in analogy with molecular crystals. Section IV gives the corresponding description for vortices on a kagomé pinning lattice. The melting of these vortex configurations and the creation of vortex plastic crystal states for both types of pinning lattices are studied in Sec. V. We construct phase diagrams for the vortex molecular crystals at the dimer and trimer fillings of the honeycomb pinning lattice as a function of temperature and pinning strength in Sec. VI. The effect of the strength of the pinning sites is explored in further detail in Sec. VII. The paper closes with a discussion in Sec. VIII and a conclusion in Sec. IX.

II. SIMULATION

We perform two-dimensional simulations of superconducting vortices in honeycomb and kagomé pinning arrays using a computational procedure similar to that previously employed for studies of vortices in square and triangular pinning arrays.[7,8,20,21] The system of size $L_x \times L_y$ has periodic boundary conditions in the x and y directions and contains

N_p pinning sites and N_v vortices. The dynamics of a vortex i located at position $\mathbf{R}_i$ is determined by the following overdamped equation of motion:

$$\eta\frac{d\mathbf{R}_i}{dt} = \mathbf{F}_i^{vv} + \mathbf{F}_i^p + \mathbf{F}_i^d + \mathbf{F}_i^T. \quad (1)$$

Here, $\mathbf{F}_i^{vv}$ is the repulsive vortex-vortex interaction force, $\mathbf{F}_i^p$ is the force from the pinning sites, $\mathbf{F}_i^d$ is the force from an external drive, and $\mathbf{F}_i^T$ is the random force from thermal fluctuations. The damping constant $\eta=\phi_0^2 d/2\pi\xi^2\rho_N$, where d is the thickness of the superconducting sample, $\phi_0=h/2e$ is the flux quantum, ξ is the superconducting coherence length, and ρ_N is the normal state resistivity of the material.[34] We measure length in units of the London penetration depth λ and for most of the results presented here, the system size is $24\lambda\times24\lambda$.

The explicit vortex-vortex interaction force is

$$\mathbf{F}_i^{vv} = \sum_{j\neq i}^{N_v} f_0 K_1\left(\frac{R_{ij}}{\lambda}\right)\hat{\mathbf{R}}_{ij}, \quad (2)$$

where K_1 is the modified Bessel function, $f_0=\phi_0^2/(2\pi\mu_0\lambda^3)$, $R_{ij}=|\mathbf{R}_i-\mathbf{R}_j|$, and $\hat{\mathbf{R}}_{ij}=(\mathbf{R}_i-\mathbf{R}_j)/R_{ij}$. A short range cutoff of 0.1λ is applied to the vortex-vortex interaction force to avoid divergence; however, at the densities considered here, vortices do not approach each other this closely. The interaction is also cut off beyond 6λ for computational efficiency since the vortex-vortex forces beyond this distance are negligible.[7] Time is measured in units of $\tau=\eta/f_0$. As an example of physical units, for a $NbSe_2$ crystal of thickness $d=0.1$ mm with $\eta=2.36\times10^{-11}$ N s/m, $f_0=6.78\times10^{-5}$ N/m and $\tau=0.35$ μs.

The pinning sites are modeled as N_p attractive parabolic traps with radius $R_p=0.3\lambda$ and strength f_p, so that

$$\mathbf{F}_i^p = -\sum_{k=1}^{N_p}\frac{f_p}{R_p}R_{ik}^{(p)}\Theta\left(\frac{R_p-R_{ik}^{(p)}}{\lambda}\right)\hat{\mathbf{R}}_{ik}^{(p)}. \quad (3)$$

Here, $\mathbf{R}_k^{(p)}$ is the location of pinning site k, $R_{ik}^{(p)}=|\mathbf{R}_i-\mathbf{R}_k^{(p)}|$, $\hat{\mathbf{R}}_{ik}^{(p)}=(\mathbf{R}_i-\mathbf{R}_k^{(p)})/R_{ik}^{(p)}$, and Θ is the Heaviside step function. The pinning radius is chosen to be small enough that only one vortex can be captured per pinning site. The pinning sites are arranged in a triangular lattice with lattice constant a_0, as illustrated in Fig. 1(a), and then 1/4 or 1/3 of the pinning sites are removed to create a kagomé or honeycomb array, as in Figs. 1(b) and 1(c). The pinning density is $n_p=N_p/(L_xL_y)$. The matching fields for the honeycomb and kagomé arrays are $B_\phi^H=n_p$ and $B_\phi^K=n_p$, respectively, while the matching field of the equivalent triangular array is B_ϕ, such that $B_\phi^H/B_\phi=2/3$ and $B_\phi^K/B_\phi=3/4$.

The driving force is assumed to arise from the application of an external current which induces a Lorentz force on the vortices that is perpendicular to the current. All vortices experience an equal driving force $\mathbf{F}^d=F^d\hat{\mathbf{x}}$ in the x direction, corresponding to the horizontal axis of Fig. 1. The thermal force $\mathbf{F}_i^T$ is modeled as random Langevin kicks with the properties $\langle\mathbf{F}_i^T\rangle=0$ and $\langle\mathbf{F}_i^T(t)\mathbf{F}_j^T(t')\rangle=2\eta k_BT\delta(t-t')\delta_{ij}$.

The initial vortex configurations are obtained by simulated annealing. Our procedure for this study was to start from an initial temperature of $F^T=3$ and decrease the temperature to $F^T=0$ in increments of $\delta F^T=0.002$ while spending 5000 simulation time steps at each increment, so that the total annealing time is 7.5×10^6 simulation time steps. We note that an overly rapid annealing rate can cause the system to be trapped in a metastable state, which prevents the vortices from ordering even at integer matching fields. To check our annealing rate, we tested slower rates and found that the resulting vortex configurations were unchanged. Once the vortex positions have been initialized and the temperature has been set to zero, we determine the velocity-force curve relations and the critical depinning force f_c by slowly increasing the external drive F^d. We measure the average vortex velocity response $V_x=N_v^{-1}\langle\Sigma_{i=1}^{N_v}\mathbf{v}_i\cdot\hat{\mathbf{x}}\rangle$, where $\mathbf{v}_i=d\mathbf{R}_i/dt$. The resulting velocity-force curve would correspond to a voltage-current curve in experiment. The depinning force is determined by applying a cutoff threshold of $V_x=0.01$ to the average velocity. We find that this cutoff is sufficiently low that the critical depinning force f_c vs B curves are not strongly sensitive to the choice of cutoff.

III. VORTEX PINNING AND ORDERING IN HONEYCOMB ARRAYS

A. Commensurability peaks at integer and half-integer fillings

We measure the critical depinning force f_c for vortices on a honeycomb pinning array with $f_p=0.5f_0$ and $B_\phi=0.47\phi_0/\lambda^2$ as a function of vortex density. The results are plotted in Fig. 2(a) as f_c/f_p versus B/B_ϕ^H, where $B_\phi^H=0.313\phi_0/\lambda^2$ is the field at which the number of vortices equals the number of pinning sites for the honeycomb pinning array. We find peaks in f_c at the integer matching fields $B/B_\phi^H=1$, 2, 3, and 4. Additionally, there are pronounced peaks in f_c at the half-matching fields $B/B_\phi^H=0.5$, 1.5, 2.5, 3.5, and 4.5. Note that the f_c peaks at the noninteger matching fields of $B/B_\phi^H=3.5$ and 4.5 are significantly larger than the peaks at the integer matching fields of $B/B_\phi^H=3$, 4, and 5, as highlighted in Fig. 2(b). There are submatching commensuration effects for $0.5<B/B_\phi^H<1.0$ which are in general weaker than the submatching commensuration effects for $B/B_\phi^H=0$ and 1.0. A similar trend was observed in earlier works for square and triangular pinning arrays.[3,8] The numerical simulations are time consuming and permit us to perform only finite field increments, so that the weaker submatching and higher order fractional matching fields are difficult to observe numerically. In this paper, we focus mainly on the pronounced matching fields.

The behavior of the commensuration effects for the honeycomb pinning lattice in Fig. 2 is very similar to the experimental results observed for honeycomb arrays in Ref. 33. In the experiments, strong commensuration effects appeared at $B/B_\phi^H=1/2$, 1, 1.5, and 2, in agreement with our results. The experiments also show that the commensuration effects at $B/B_\phi^H=3$ and 4 are very weak or absent, while those at $B/B_\phi^H=3.5$ and 4.5 are very pronounced. This is also in agreement with our result, as seen in Fig. 2(b). One differ-

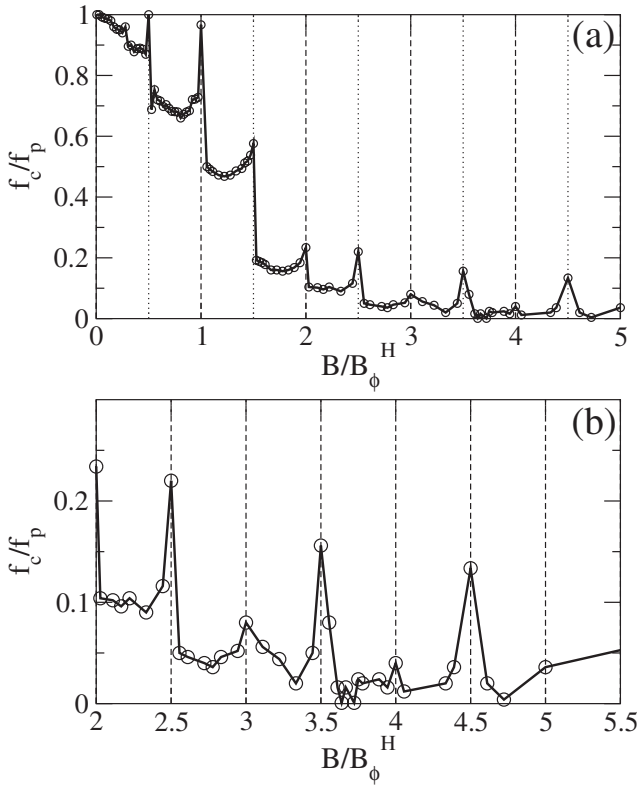

FIG. 2. (a) The depinning force f_c/f_p vs B/B_ϕ^H for the honeycomb pinning array illustrated in Fig. 1(c) with $f_p=0.5f_0$, $B_\phi=0.47\phi_0/\lambda^2$, and $B_\phi^H=0.313\phi_0/\lambda^2$. (b) A blow-up from (a) of f_c/f_p vs B/B_ϕ^H in the region $B/B_\phi^H \geq 2$.

ence between the experimental results and our work is that we find a very pronounced peak in f_c at $B/B_\phi^H=2.5$, while the experiments produced only a weak peak at the same field. In Sec. V, we show that this may be due to the fact that the commensurate vortex configuration at $B/B_\phi^H=2.5$ is unstable under thermal fluctuations.

Figure 3 shows a comparison between the behavior of f_c as a function of B for the honeycomb pinning array (heavy line) and a triangular pinning array with the same value of $B_\phi=0.47\phi_0/\lambda^2$ (light line). The depinning force f_c for the triangular pinning array exhibits pronounced peaks at $B/B_\phi=1/3$, 2, and 3 and only very weak peaks at noninteger matching fields for $B/B_\phi>1$. The peak at the second matching field $B/B_\phi=2$ for the triangular pinning array is significantly smaller than the one at the third matching field $B/B_\phi=3$. This effect has been observed in previous studies and results from the fact that the vortex lattice forms a honeycomb structure at the second matching field, while at the third matching field the overall symmetry of the vortex lattice is triangular.[7] Figure 3 also indicates that the peak at $B/B_\phi=1.0$ for the triangular array coincides with the peak at $B/B_\phi^H=1.5$ for the honeycomb array, while a peak at $B/B_\phi=1/3$ in the triangular array coincides with a peak at $B/B_\phi^H=1/2$ in the honeycomb array.

B. Vortex configurations for $B \leqslant B_\phi$

In order to explain the origin of the pronounced commensurability peaks in f_c for the honeycomb pinning array at

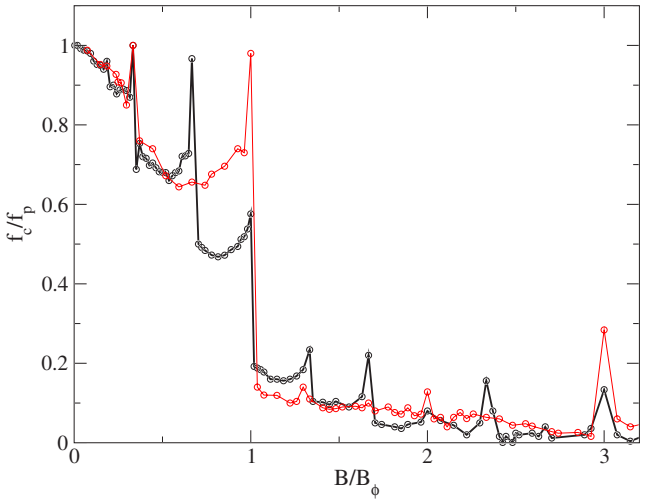

FIG. 3. (Color online) f_c/f_p vs B/B_ϕ for the honeycomb pinning array (black heavy line) and the triangular pinning array (red light line) in Figs. 1(a) and 1(c) with $f_p=0.5f_0$ and $B_\phi=0.47\phi_0/\lambda^2$.

$B/B_\phi^H=n/2$ and the fact that some peaks are more prominent than others, we analyze the vortex configurations at these fields. In the left panels of Fig. 4, we illustrate the vortex and pinning site locations for three matching fields in the honeycomb array from Fig. 2, while the right panels of Fig. 4 show only the vortex positions at the same fields in order to emphasize the vortex lattice structure.

Figures 4(a) and 4(b) indicate that at $B/B_\phi^H=1/2$, the overall vortex lattice is triangular. The vortex configuration at half filling for the honeycomb lattice is the same as that of vortices at unit filling in an undiluted triangular lattice with matching field $B_\phi^H/2$ that is rotated by 90° relative to the triangular lattice in Fig. 1(a). The configuration is also identical to the vortex arrangement found for 1/3 filling of a triangular lattice with matching field B_ϕ.[8] Since the vortex lattice structure is triangular, the vortex-vortex interactions cancel and the depinning force is determined only by the maximum force of the pinning sites such that $f_c/f_p=1.0$. This is what we find at $B/B_\phi^H=1/2$, as seen in Fig. 2. For fields just above or below half filling, the vortex lattice retains the same triangular ordering shown in Figs. 4(a) and 4(b) but contains weakly pinned vacancies or interstitials which reduce the value of f_c. In the case of a triangular pinning array, there is no commensurate peak at $B/B_\phi=1/2$ when all of the vortices are forced to occupy pinning sites since the system is geometrically frustrated, resulting in a strongly defected vortex lattice.[8] If f_p is very weak, an ordered vortex lattice can form at this field when the elastic forces of the vortex lattice overcome the pinning force, allowing half of the vortices to shift out of the pinning sites and creating a partially pinned or floating triangular vortex lattice.[8,30] In our simulations, the pinning strength $f_p=0.5f_0$ is well above this limit so that floating vortex configurations do not occur; we return to this point in Secs. VI and VII. We note that for very low applied fields $B/B_\phi \ll 1$, the depinning force is dominated by single vortex pinning and thus $f_c/f_p \approx 1$.

The vortex configuration for the first matching field in the honeycomb array, $B/B_\phi^H=1$, is illustrated in Figs. 4(c) and

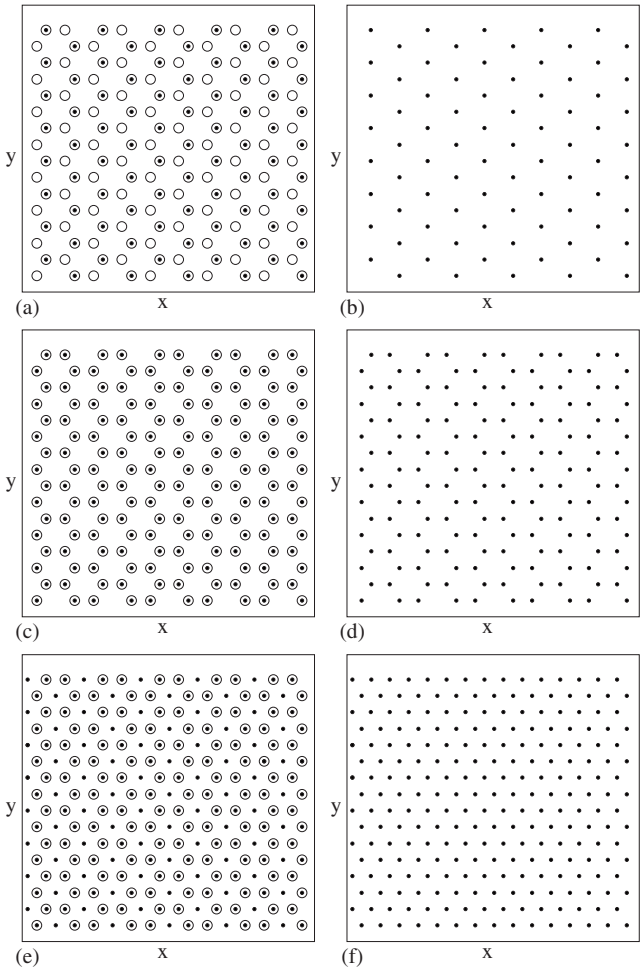

FIG. 4. Left panels: vortex positions (black dots) and pinning site positions (open circles) obtained for the honeycomb array in Figs. 1(c) and 2. Right panels: vortex positions only. [(a) and (b)] $B/B_\phi^H=1/2$. [(c) and (d)] $B/B_\phi^H=1$. [(e) and (f)] $B/B_\phi^H=1.5$.

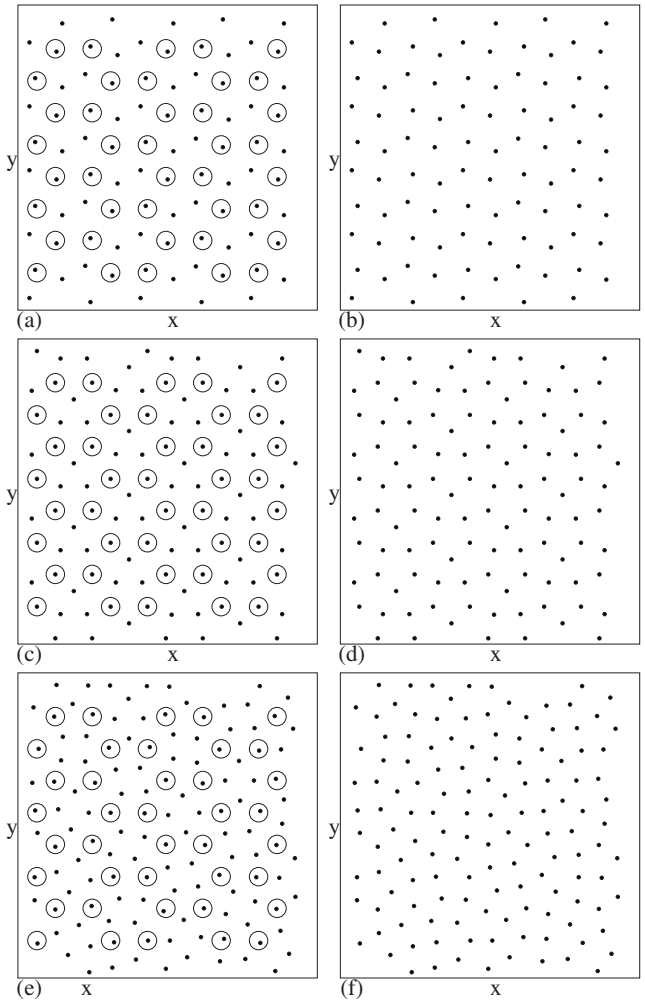

FIG. 5. Left panels: vortex positions (black dots) and pinning site positions (open circles) in a portion of the sample for the honeycomb pinning array from Figs. 1(c) and 2. Right panels: Vortex positions only. [(a) and (b)] $B/B_\phi^H=2.0$. [(c) and (d)] $B/B_\phi^H=2.5$. [(e) and (f)] $B/B_\phi^H=3.0$.

4(d). The vortex lattice has the same highly symmetric structure as the pinning lattice and as a result the vortex-vortex interactions cancel, giving $f_c/f_p=1.0$, as shown in Fig. 2. For fields above the first matching field, the additional N_v-N_p vortices are located in the interstitial regions and are pinned not by the pinning sites but by the interactions with the vortices trapped at the pinning sites. In general, this interstitial pinning is weak, so f_c/f_p drops significantly for $B/B_\phi^H>1.0$, as seen in Fig. 2.

At $B/B_\phi^H=1.5$, where a prominent peak in the depinning force appears in Fig. 2, the overall vortex lattice is triangular, as shown in Figs. 4(e) and 4(f). In this case, the interstitial sites that were produced when the triangular pinning array was diluted to form the honeycomb pinning array each capture one vortex. Figure 3(b) shows that the prominent peak in f_c/f_p at $B/B_\phi=1$ for the triangular pinning array coincides with the peak at $B/B_\phi^H=1.5$ in the honeycomb pinning array. Although the symmetry of the vortex lattice is triangular in each case, at $B/B_\phi^H=1.5$ for the honeycomb pinning array, the depinning force is determined not by f_p but by the caging force on the vortices in the interstitial regions. As a result, the depinning force for the honeycomb array at this field is lower than the depinning force for the triangular array at $B/B_\phi=1.0$ filling, as seen in Fig. 3(b). For fields slightly below or above $B/B_\phi^H=1.5$ in the honeycomb pinning array, interstitials or vacancies appear in the triangular vortex lattice at the locations of the missing pins and cause a reduction in f_c/f_p.

C. Vortex configurations for $B>B_\phi$

As B increases above $B/B_\phi^H=1.5$, the additional vortices sit in the large interstitial regions at the center of each honeycomb plaquette. In general, for $1.5<B/B_\phi^H<2.0$, we find that the plaquette centers capture at most two vortices rather than three. The two vortices cannot both sit at the center of the interstitial site, so instead they form an interstitial dimer state, as illustrated in Figs. 5(a) and 5(b) at $B/B_\phi^H=2.0$. The interstitial dimers have an additional orientational ordering which is highlighted in Figs. 5(a). The dimers can be described as having a director field which is oriented at a 30°

angle with the x axis in Figs. 5(a) and 5(b). Within the center interstitial region of each honeycomb plaquette, the six surrounding pinned vortices create a sixfold modulated symmetric potential and each vortex forming the interstitial dimer sits in one of the minima of this potential. As a result, at zero temperature each dimer can be oriented in one of three degenerate directions. If we change the initial conditions during the simulated annealing process slightly, we find the same configuration shown in Figs. 5(a) and 5(b) with one-third probability. With equal probabilities, we obtain configurations in which all the dimers are either oriented at 90° or −30° angles with the x axis. If the dimers in neighboring plaquettes did not interact with each other we would expect to find a random distribution of dimer orientations among the three degenerate directions in a given configuration. The orientational ordering of the dimers in our system indicates that dimers in neighboring plaquettes do interact with each other and that this interaction gives the dimers a ferromagneticlike alignment. Unlike an Ising model in zero magnetic field which has two possible spin orientations, this system has three possible orientations for the dimers and is thus more closely related to a three-state Potts model. The ordering of the dimers is very similar to the ordering found in the recently studied model of colloidal dimers on a triangular lattice, which has been shown to map to the three-state Potts model.[28] The theoretical work in Ref. 28 indicates that the dimers lose their orientational ordering as a function of temperature through either a continuum melting transition or a first order transition, depending on the system parameters. The colloidal dimers in neighboring plaquettes have been shown to interact through an effective quadrupole moment with an additional screening term;[27] higher order n-mers were also considered which interact through higher order pole moments. These types of interactions are anisotropic and thus the pole moment energy can be minimized when the n-mers form an orientationally ordered state. Neighboring dimers may be oriented parallel or perpendicular to each other depending on the pinning geometry.[25] The colloids interact via a repulsive screened Yukawa potential; since this is similar to the vortex interaction of Eq. (2), the same type of multipole interactions between vortices in neighboring plaquettes should emerge as in the colloid system.

For fields $2.0 < B/B_\phi^H < 2.5$, the additional vortices again occupy the interstitial sites where they form trimer states. For this range of fields, we do not find any interstitial sites that have captured four vortices. Figure 5(c) shows the vortex configuration at $B/B_\phi^H = 2.5$ where each pinning site captures one vortex and each center interstitial region captures three vortices. The trimers are equilateral triangles and each vortex in the trimer is located at one of the sixfold potential minima created by the six surrounding pinned vortices. In the same manner as the dimer states, the trimers are orientationally ordered and all align in one of the two possible degenerate orientations, indicating that neighboring trimers have an interaction with ferromagnetic character. The overall vortex lattice structure at $B/B_\phi^H = 2.5$ is very intricate, as indicated in Fig. 5(d). It can be viewed as triangles of vortices each surrounded by three pentagons, indicating that a large fraction of the system has fivefold ordering coexisting with true long-range order.

Figure 5(e) illustrates the vortex configurations and pinning site locations at $B/B_\phi^H = 3.0$. At this filling, a weak peak in f_c/f_p appears, as shown in Fig. 2. Here, each pinning site captures one vortex and the center interstitial regions capture four vortices in a quadrimer state. Unlike the dimers and trimers, we find no orientational ordering of the quadrimers. The fourfold symmetry of the quadrimer state cannot match the sixfold modulation of the potential at the center of the honeycomb plaquette. If the four vortices in the quadrimer sit at minima of this potential, then at least two vortices must occupy adjacent minima, which is energetically unfavorable due to the vortex-vortex interactions. Instead, the quadrimers form distorted square structures that are not commensurate with the underlying sixfold modulated potential. Since the overall orientational order of the quadrimers is absent at the $B/B_\phi^H = 3.0$ filling, a strong commensurate peak in f_c/f_p does not occur. A weak peak does appear at this filling, as seen in Fig. 2, due to the fact that each interstitial region captures exactly four vortices at $B/B_\phi^H = 3.0$. Just above or below this field, vacancies or interstitials in the form of threefold or fivefold occupied interstitial sites occur, which are less strongly pinned and cause a reduction in f_c.

In Figs. 6(a) and 6(b), we show the vortex configurations at $B/B_\phi^H = 3.5$ where a strong peak in f_c/f_p appears in Fig. 2(b). At this field, the system deviates from the pattern which we observed at lower fields for $n = 1-4$ of forming symmetrical n-mers in the interstitial sites at the center of the honeycomb plaquettes. Instead of forming a pentamer state at $B/B_\phi^H = 3.5$, the interstitial vortices are arranged with four vortices captured as a rectangular quadrimer in the center of each interstitial plaquette and a fifth vortex between two adjacent pinned vortices. The vortex lattice has long-range order with all the center quadrimers aligned in the same direction, unlike the $B/B_\phi^H = 3.0$ filling of Figs. 5(e) and 5(f). The ordering is possible because the fifth interstitial vortex which sits at the boundary of the honeycomb plaquette breaks the sixfold symmetry of the potential minima inside the center of the plaquette and replaces it with a twofold symmetry which can be matched by the remaining quadrimer of interstitial vortices.

At $B/B_\phi^H = 4.0$, a small commensuration peak appears in Fig. 2(b). The corresponding vortex configuration is illustrated in Figs. 6(c) and 6(d). The vortex lattice has long-range order. Each interstitial site captures six vortices in the form of an inverted triangular structure with three interstitial vortices at the top, two in the middle, and one at the bottom. The triangles have a twofold degenerate ordering, and we have also observed the other possible ordering in which each triangle points upward instead of downward along the y direction. Although the vortex lattice structure has long-range order at $B/B_\phi^H = 4.0$, there is not a large increase in f_c/f_p at this field. This may be due to the fact that the triangular configuration of interstitial vortices is unstable to fluctuation effects, as we will describe in Sec. V.

In Figs. 6(e) and 6(f), we illustrate the vortex configuration at $B/B_\phi^H = 4.5$ where a pronounced peak in the depinning force occurs in Fig. 2(b). In this case, the seven interstitial vortices captured in each interstitial site are arranged with one vortex in the center surrounded by six interstitial vortices sitting in the sixfold potential minima created by the six

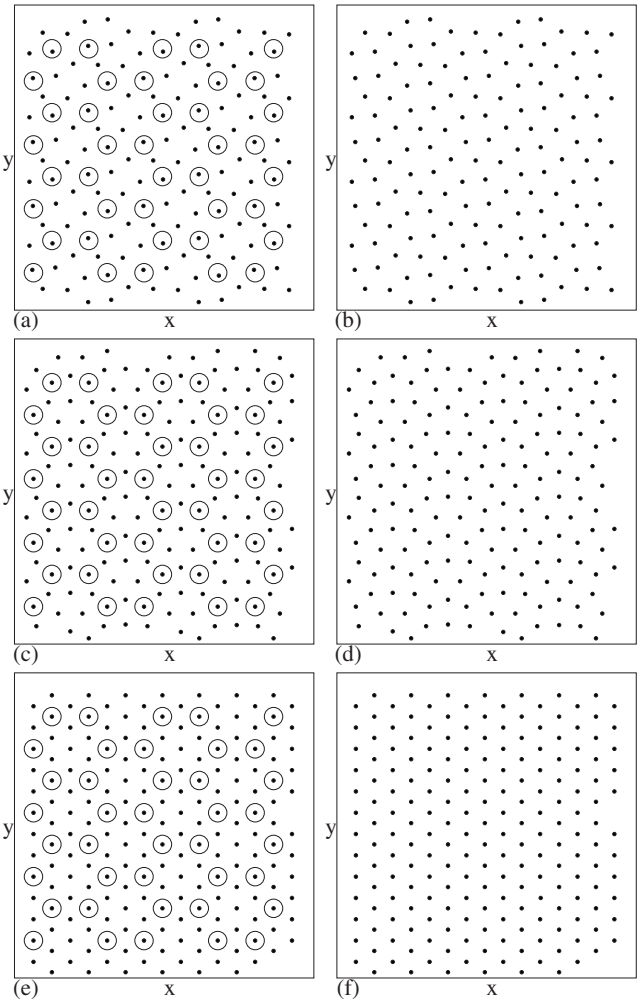

FIG. 6. Left panels: Vortex positions (black dots) and pinning site positions (open circles) in a portion of the sample for the honeycomb array from Fig. 1(c) and Fig. 2. Right panels: vortex positions only. (a,b) $B/B_\phi^H=3.5$. (c,d) $B/B_\phi^H=4.0$. (e,f) $B/B_\phi^H=4.5$.

neighboring pinned vortices. The overall vortex lattice has a triangular ordering, as seen in Fig. 6(f), and the vortex configuration is the same as that which would result at $B/B_\phi=3.0$ for a triangular pinning array that is rotated by 90° relative to the triangular lattice in Fig. 1(a), where the center interstitial vortex would be located in a pinning site. For $B/B_\phi^H=5.0$ (not shown), we find a state without orientational order and there is no particular peak in f_c/f_p at this field. We note that for very high applied fields $B/B_\phi^H \gg 1$, the depinning response is dominated by the shearing motion of the interstitial vortices.

As we have demonstrated, the honeycomb array can stabilize various types of interstitial vortex n-mer states at the center of each honeycomb plaquette. These n-mers have a tendency to align in the same direction, indicating effective ordering of a ferromagnetic nature which is similar to the ordering observed for colloidal n-mer states on periodic substrates. At fields $B/B_\phi^H=n/2$ where an ordered vortex crystal forms, we observe peaks in the depinning force. As we describe in further detail in Sec. V, we find that at finite and increasing temperature, a melting transition can occur in

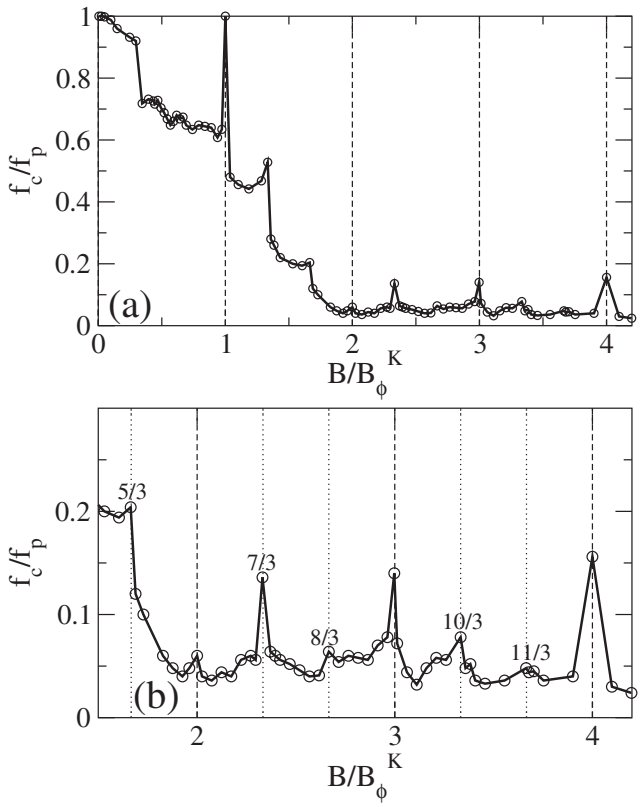

FIG. 7. (a) The depinning force f_c/f_p vs B/B_ϕ^K for the kagomé pinning array illustrated in Fig. 1(b) with $f_p=0.5f_0$, $B_\phi=0.47\phi_0/\lambda^2$, and $B_\phi^K=0.3525\phi_0/\lambda^2$. (b) A blow-up from (a) of f_c/f_p vs B/B_ϕ^K in the region $B/B_\phi^K>2.0$.

which the n-mers lose their orientational ordering but remain trapped in the center interstitial regions of each honeycomb plaquette, similar to the vortex dimer states in kagomé arrays[31] and the colloidal n-mer molten states.[25,26,28] This suggests that many of the spin model analogies developed to describe orientational ordering of colloidal n-mer states can be applied to the vortex n-mers as well. We term the orientationally ordered vortex n-mer states "vortex molecular crystals" in analogy with molecular crystals, which have translational order along with an additional alignment of the molecules. At higher temperatures where the molecules lose their orientational ordering but remain in translationally ordered lattice positions, the system is referred to as a plastic crystal. Thus, by analogy, states such as that in Fig. 5(e) would be a vortex plastic crystal. The high temperature states (described in Sec. V) in which the orientational ordering has melted at $B/B_\phi^H=2$, 2.5, and 3.5 would also be plastic vortex crystals.

IV. VORTEX STATES AND COMMENSURABILITY IN KAGOMÉ ARRAYS

A. Commensurability peaks at integer and $B/B_\phi^K=n/3$ fillings

In Fig. 7(a), we plot f_c/f_p obtained for vortices interacting with the kagomé pinning array illustrated in Fig. 1(b) with $f_p=0.5f_0$, $B_\phi=0.47\phi_0/\lambda^2$, and $B_\phi^K=0.3525\phi_0/\lambda^2$, where B_ϕ^K

is the field at which the number of vortices equals the number of pinning sites in the kagomé array. Unlike the honeycomb array, there is no strong peak in f_c/f_p at $B/B_\phi^K=1/2$ or at any of the submatching fields $B/B_\phi^K<1$ for the kagomé array, but clear commensurability peaks occur at the integer matching fields $B/B_\phi^K=1$, 2, 3, and 4. In addition to the integer peaks, there are a series of peaks at $B/B_\phi^K=n/3$ for $n>3$. The strongest of these peaks fall at $B/B_\phi^K=4/3$, 5/3, 7/3, and 10/3, as shown in Fig. 7(b). The existence of clear fractional matching effects at fields above the first matching field is similar to the behavior seen in the honeycomb pinning array (Fig. 2) and distinct from the behavior of a triangular pinning array (Fig. 3), where no strong fractional matching effects appear above $B/B_\phi=1$. This indicates that the pinning behavior of the kagomé and honeycomb pinning arrays is very similar and suggests that similar types of orientationally ordered vortex molecular crystal states are occurring in the kagomé array as in the honeycomb array.

B. Vortex configurations for $B \leqslant B_\phi$

In Figs. 8(a) and 8(b), we show the vortex configuration for the kagomé pinning array from Fig. 7 at $B/B_\phi^K=1/3$. Here, the vortex lattice does not order and in general we do not observe any particularly ordered vortex lattices for the submatching fields $B/B_\phi^K<1$ for the kagomé pinning arrays, in contrast to the triangular and honeycomb pinning arrays. In the honeycomb pinning array, Fig. 2(a) showed that there is a peak in f_c/f_p at $B/B_\phi^H=1/3$ followed by a drop in f_c/f_p. For the kagomé pinning, Fig. 7 indicates that although there is no peak in f_c/f_p at $B/B_\phi^K=1/3$, there is still a drop in f_c/f_p at this field. In each case, the drop in f_c/f_p occurs due to a change in the nature of the vortex-vortex interactions. For fields at and below 1/3 filling, the spacing between adjacent vortices is at least $2a_0$ and the vortex-vortex interactions are minimal. For fields above 1/3 filling, in order for all of the vortices to occupy pinning sites, some of the vortices must be located at a distance of a single lattice constant a_0 from another vortex, while the spacing between other nearest-neighboring vortices remains the larger distance $2a_0$. A vortex which has some nearest neighbors at a distance a_0 and other nearest neighbors at a distance $2a_0$ experiences an asymmetric vortex-vortex interaction force. This asymmetry causes the vortex to depin at a significantly lower driving force, producing the drop in f_c/f_p above 1/3 filling.

At $B/B_\phi^K=1.0$ where each pinning site captures one vortex, the net vortex symmetry is that of a kagomé lattice, as indicated in Figs. 8(c) and 8(d). At $B/B_\phi^K=4/3$, shown in Figs. 8(e) and 8(f), each center interstitial site of the kagomé plaquettes captures one vortex so that the overall vortex configuration is triangular. This vortex configuration is the same as that for the triangular pinning lattice in Fig. 1(a) at $B/B_\phi=1$, where the vortices at interstitial locations in the kagomé lattice would sit in pinning sites in the triangular pinning lattice. The $B/B_\phi^K=4/3$ filling also corresponds to the $B/B_\phi^H=1.5$ filling of the honeycomb array where each interstitial site captures one vortex and to the "first" matching field of Ref. 31. For the kagomé lattice at $B/B_\phi^K \ll 1$, single vortex depinning dominates the response of the system and $f_c/f_p \approx 1$.

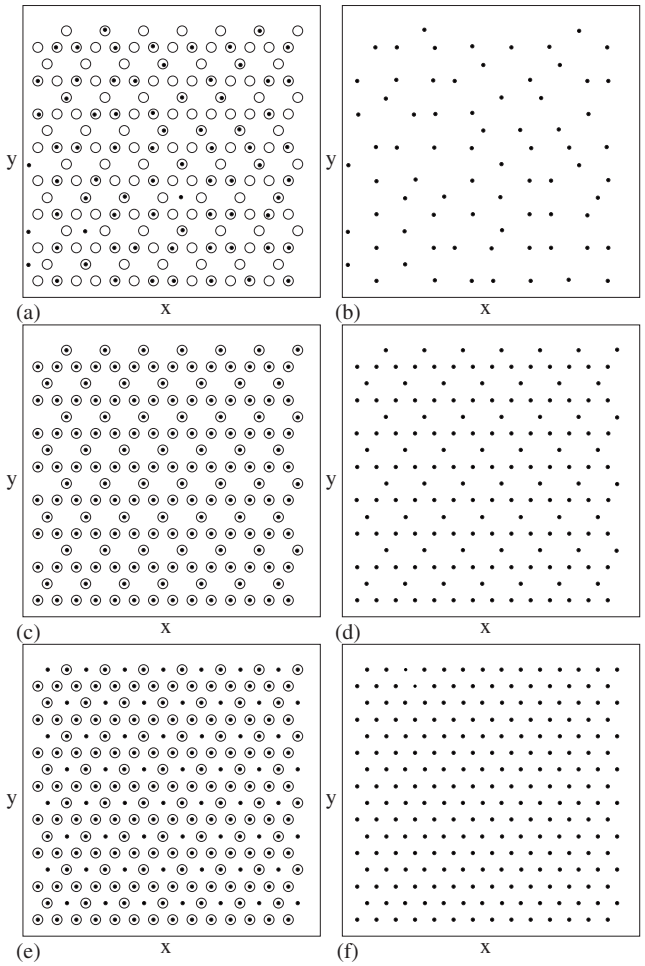

FIG. 8. Left panels: vortex positions (black dots) and pinning site locations (open circles) obtained for the kagomé array in Figs. 1(b) and 7. Right panels: vortex positions only. [(a) and (b)] $B/B_\phi^K=1/3$. [(c) and (d)] $B/B_\phi^K=1.0$. [(e) and (f)] $B/B_\phi^K=4/3$.

C. Vortex configurations for $B > B_\phi$

Figures 9(a) and 9(b) illustrate the vortex configuration at $B/B_\phi^K=5/3$ in the kagomé pinning array. At this filling, each interstitial site at the center of the kagomé plaquettes captures two vortices which form a dimerized state, as highlighted in Fig. 9(a). Unlike the dimerized state in the honeycomb pinning array where the dimers are all aligned in the same direction, in the kagomé array the dimers are tilted in opposite directions from one row to the next. This type of dimer structure is referred to as a herringbone state and has been observed for colloidal dimers on triangular arrays[25,28] as well as for the deposition of molecular dimers on triangular substrates[35] and in three-state Potts models.[36]

At $B/B_\phi^K=2.0$, each central interstitial site captures three vortices which form a trimer state, as shown in Figs. 9(c) and 9(d). The trimer orientation is twofold degenerate as in the honeycomb array, and the trimers are oriented pointing either up or down. Figure 9(c) shows that the up-down ordering is neither random nor uniform but occurs in domains reminiscent of an Ising model in zero field where domain walls have formed. If the domain wall energy is low, the relaxation time

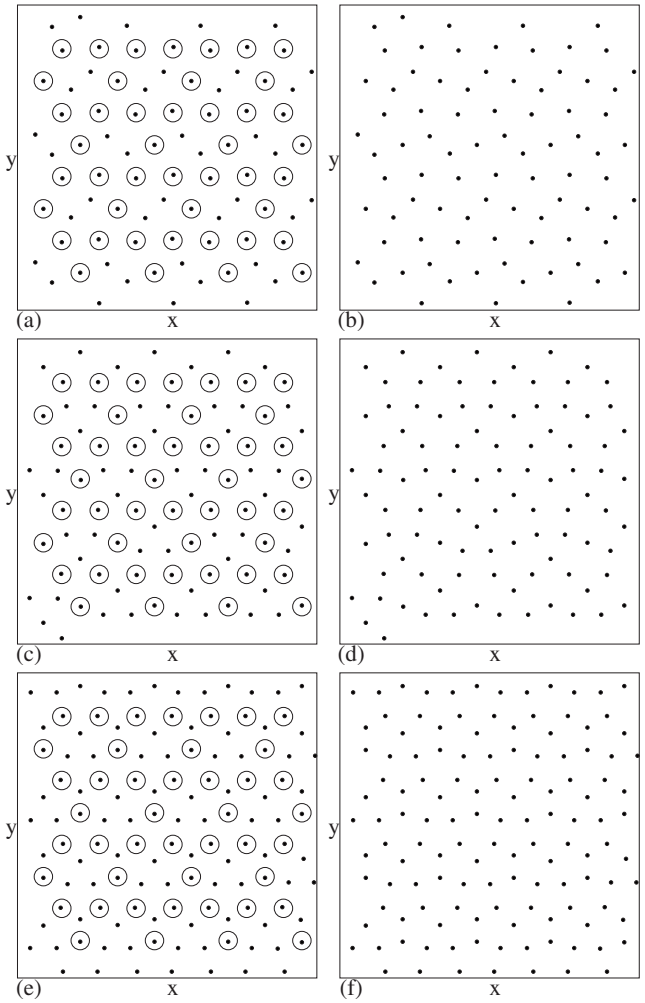

FIG. 9. Left panels: vortex positions (black dots) and pinning site locations (open circles) in a portion of the sample for the kagomé array from Fig. 7. Right panels: vortex positions only. [(a) and (b)] $B/B_\phi^K=5/3$. [(c) and (d)] $B/B_\phi^K=2.0$. [(e) and (f)] $B/B_\phi^K=7/3$.

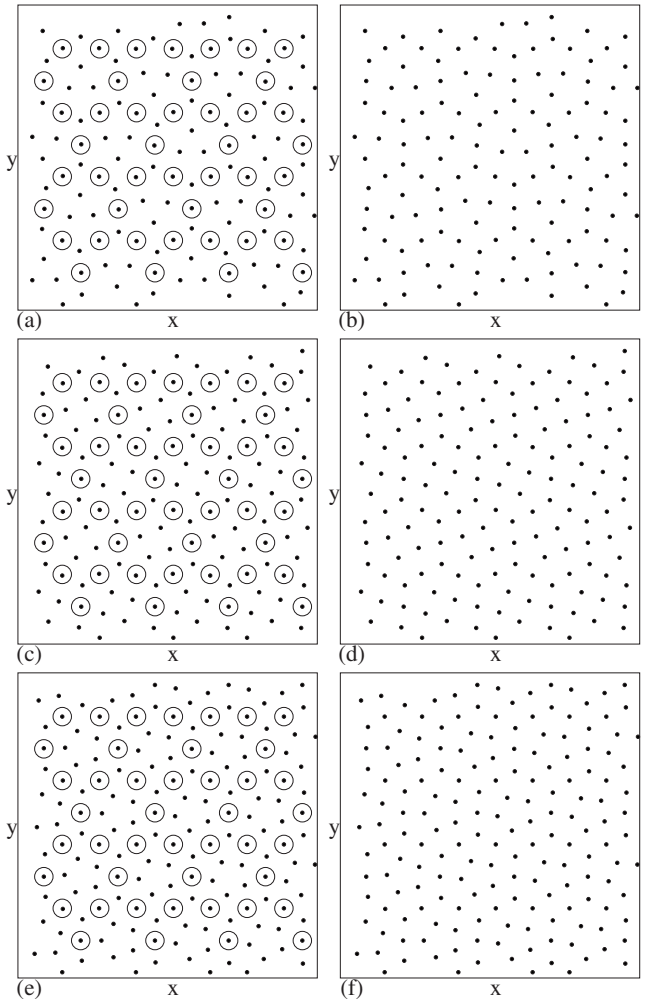

FIG. 10. Left panels: vortex positions (black dots) and pinning site locations (open circles) in a portion of the sample for the kagomé array from Fig. 7. Right panels: vortex positions only. [(a) and (b)] $B/B_\phi^K=8/3$. [(c) and (d)] $B/B_\phi^K=3$. [(e) and (f)] $B/B_\phi^K=10/3$.

to reach a state where one of the phases dominates can be exceedingly long, and here we find that it is beyond our computational time scale. In spite of the lack of true long range order, a small peak still appears in f_c/f_p at this filling, as seen in Fig. 7(b).

In Figs. 9(e) and 9(f) at $B/B_\phi^K=7/3$, the large interstitial sites in the kagomé plaquette centers again capture three vortices and the additional fourth interstitial vortex is located in the small interstitial space between three pinning sites. Only half of the small interstitial regions capture a vortex. The trimers in the large interstitial sites are all aligned in the same direction, in contrast to the mixture of alignments found at $B/B_\phi^K=2.0$ in Figs. 9(c) and 9(d). The presence of the fourth interstitial vortex in the small interstitial sites breaks the sixfold symmetry of the large interstitial region and produces only a single low-energy alignment direction for the interstitial trimer. A grain boundary would require a shift in the position of the vortices in the small interstitial sites as well as a change in the orientation of the trimers. Such a grain boundary has a high energy and is not stable in our simulation. Since there are no grain boundaries present, this state has long-range orientational order, and as a result the peak in f_c/f_p at $B/B_\phi^K=7/3$ shown in Fig. 7 is higher than the peaks at $B/B_\phi^K=2.0$ and $B/B_\phi^K=8/3$, where the vortices do not form completely orientationally ordered states.

A related state appears at $B/B_\phi^K=8/3$, shown in Figs. 10(a) and 10(b), where the large interstitial site captures three vortices in a trimer state and all, rather than half, of the small interstitial sites capture one vortex. This state was termed the "second" matching field in Ref. 31. Since all of the small interstitial sites are now occupied, the sixfold symmetry of the potential in the large interstitial sites is restored, resulting in two degenerate orientations for each trimer. The interaction between neighboring trimers is not strong enough to induce a global orientation of the trimers, so, as shown in Figs. 10(a) and 10(b), there is no long-range trimer orientational order at $B/B_\phi^K=8/3$, just as there was no long-range orientational order at $B/B_\phi^K=2.0$ in Figs. 9(c) and 9(d). There is also only a small peak in f_c/f_p at $B/B_\phi^K=8/3$, as seen in Fig. 7(b).

For $B/B_\phi^K=3.0$, illustrated in Figs. 10(c) and 10(d), the large interstitial region captures four vortices which form a quadrimer state. The remaining interstitial vortices fill all of the small interstitial sites. The quadrimers are orientationally ordered and have an effective herringbone structure in which the quadrimers are tilted in opposite directions from one row to the next. This state might more appropriately be called a double herringbone since the herringbone state is composed of single dimers, while here two dimers have been paired to form a quadrimer. As mentioned earlier, herringbone states appear in surface physics for the deposition of molecular dimers on triangular substrates.[35] We are not aware of any observation of the double herringbone structure for surface ordering. Such states might occur for the deposition of cubic molecules on triangular surfaces. Figure 7 shows that there is a prominent peak in f_c/f_p at $B/B_\phi^K=3.0$ due to the overall orientational ordering of the quadrimer state.

An ordered state also forms at $B/B_\phi^K=10/3$, as shown in Figs. 10(e) and 10(f). Each large interstitial region captures five vortices which form a pentagon and the smaller interstitial sites all capture one vortex. The interstitial pentagons are aligned in a single direction, as indicated in Fig. 8(e). In surface physics, it is uncommon to consider fivefold symmetric molecules that form a pentagon; however, if such ring-type molecules occur and lie flat on an atomic surface, then a similar ordering may appear.

There is no appreciable peak in f_c/f_p at $B/B_\phi^K=11/3$ in Fig. 7. The vortex configuration corresponding to this field is plotted in Figs. 11(a) and 11(b). All of the small interstitial sites are occupied, while some of the large interstitial sites capture seven interstitial vortices and the rest capture five vortices. The resulting vortex structure has no long-range orientational order. In general, we do not observe states where six vortices are captured in the large interstitial regions. The triangular six-vortex configuration that appears in the honeycomb pinning lattice in Fig. 6(c) at $B/B_\phi^H=4$ is not stable for the kagomé pinning lattice due to the presence of the vortices in the small interstitial sites. At $B/B_\phi^K=4.0$, which was termed the "third" matching field in Ref. 31, Figs. 11(c) and 11(d) show that each large interstitial region captures seven vortices and the remaining interstitial vortices fill the small interstitial sites. The overall vortex lattice is triangular and a prominent peak in f_c/f_p is observed at this filling, as seen in Fig. 7. For higher fillings, we find additional ordered and disordered states and, in Figs. 11(e) and 11(f), we show the case of $B/B_\phi^K=16/3$ where a triangular vortex lattice forms. At very high fillings $B/B_\phi^K \gg 1$, depinning occurs via a shearing motion of the interstitial vortices.

These results indicate that the kagomé pinning array produces peaks in the critical current at most fields $B/B_\phi^K=n/3$ for $n>3$. In some cases such as $B/B_\phi^K=8/3$ and $B/B_\phi^K=11/3$, the peaks are missing or strongly reduced due to a lack of orientational ordering in the vortex configuration. The general behavior for both the honeycomb and kagomé pinning arrays is very similar in that n-mer states with various types of orientational ordering form in the large interstitial regions of the pinning lattice.

V. VORTEX PLASTIC CRYSTAL STATES

As noted in Sec. III C, the orientationally ordered dimer and higher order n-mer states that form in the large interstitial regions of the honeycomb and kagomé pinning lattices are very similar to the colloidal molecular crystals studied recently.[25,26,28] Colloidal molecular crystals undergo a thermal disordering transition to a state in which the orientational ordering of the n-mers is lost when the n-mers remain localized at the lattice sites but begin to rotate freely.[25,26,28] Here, we show that the vortex n-mers exhibit a similar rotational melting behavior.

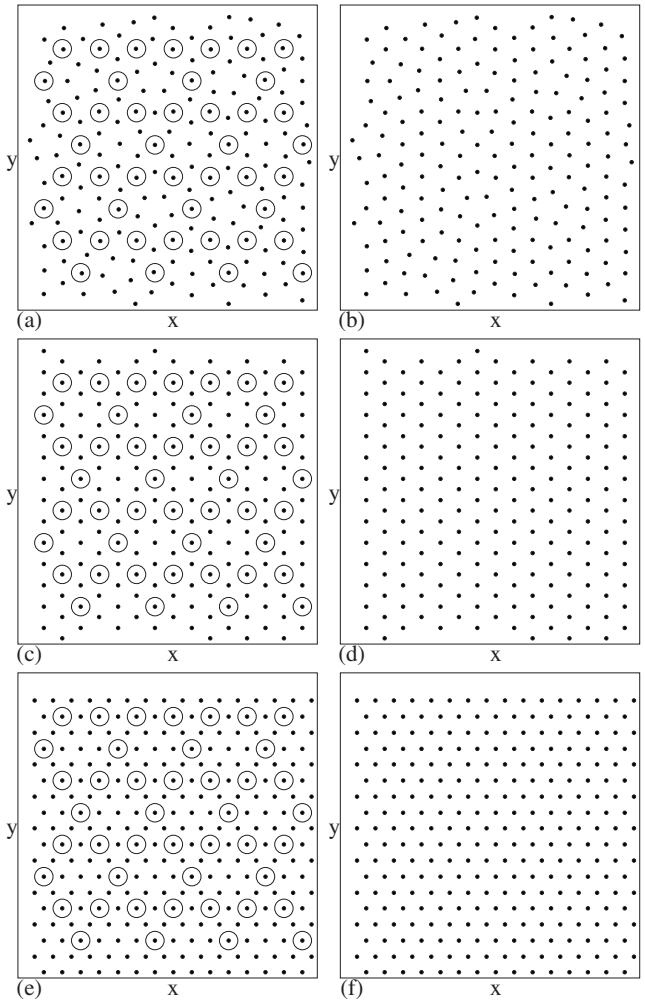

FIG. 11. Left panels: vortex positions (black dots) and pinning site locations (open circles) in a portion of the sample for the kagomé array from Fig. 7. Right panels: vortex positions only. [(a) and (b)] $B/B_\phi^K=11/3$. [(c) and (d)] $B/B_\phi^K=4$. [(e) and (f)] $B/B_\phi^K=16/3$.

In Fig. 12(a), we plot the vortex positions and pinning site locations for the honeycomb pinning array in Figs. 5(a) and 5(b) at $B/B_\phi^H=2$ and temperature $F^T=1.56$. At $F^T=0$ in Fig. 5(a), the dimers are all aligned in a single direction, but at $F^T=1.56$ in Fig. 12(a), the dimer alignment is lost, although the dimers remain confined to the interstitial sites. The vortex trajectories, illustrated in Fig. 12(b) for a period of 10^3 simulation time steps, indicate that while the pinned vortices move a small amount, each dimer is undergoing rotational motion between the three low-energy orientations. We find that there is some correlation in the dimer motions; however, over long distances, the true long-range orientational order-

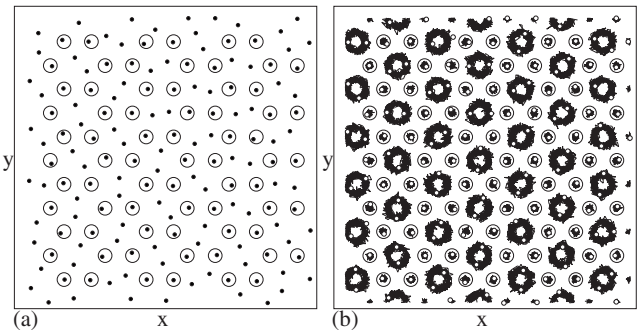

FIG. 12. (a) The vortex positions (black dots) and pinning site locations (open circles) in a portion of the sample for the honeycomb pinning array in Figs. 5(a) and 5(b) with $f_p=0.5f_0$ and $B/B_\phi^H=2.0$ at a temperature of $F^T=1.56$. (b) The same as in (a) with vortices (white dots), pinning sites (open circles), and vortex trajectories (black lines) over a fixed time period of 10^3 simulation time steps.

ing is lost. We refer to this finite temperature state with no orientational order as a "vortex plastic crystal" since it is similar to the colloidal plastic crystal phases. In the vortex dimer case, there are two species of vortices: the interstitial dimers and the single vortices trapped at the pinning sites. In the colloidal system of Refs. [25,26,28], the egg-carton substrate does not allow interstitial colloids to exist so there is only a single species of n-mer states.

In Fig. 13(a), we plot the fraction of orientationally ordered dimers P as a function of temperature F^T for the honeycomb pinning lattice at $B/B_\phi^H=2$ from Fig. 12. To determine P, for each dimer we identify the angle α which the line connecting the two vortices composing the dimer makes with the positive x axis, where $0\leqslant\alpha<180°$. We then assign a state d_i to each dimer of 1, 2, or 3 depending on whether α is closest to 30°, 90°, or 120°. The ordered fraction P is given by $P=N_d^{-1}\max[\Sigma_{i=1}^{N_d}\delta(1-d_i),\Sigma_{i=1}^{N_d}\delta(2-d_i),\Sigma_{i=1}^{N_d}\delta(3-d_i)]$, where N_d, is the number of dimers in the sample. For $F^T\leqslant 1.25$, the dimers remain orientationally ordered with $P=1$ and form the vortex molecular crystal state shown in Fig. 5(a). For $1.25<F^T\leqslant 2.3$, the orientational order is thermally destroyed and the system enters the vortex plastic crystal state. For $F^T>2.3$, the dimers break apart, P is no longer defined, and there is vortex diffusion throughout the entire system.

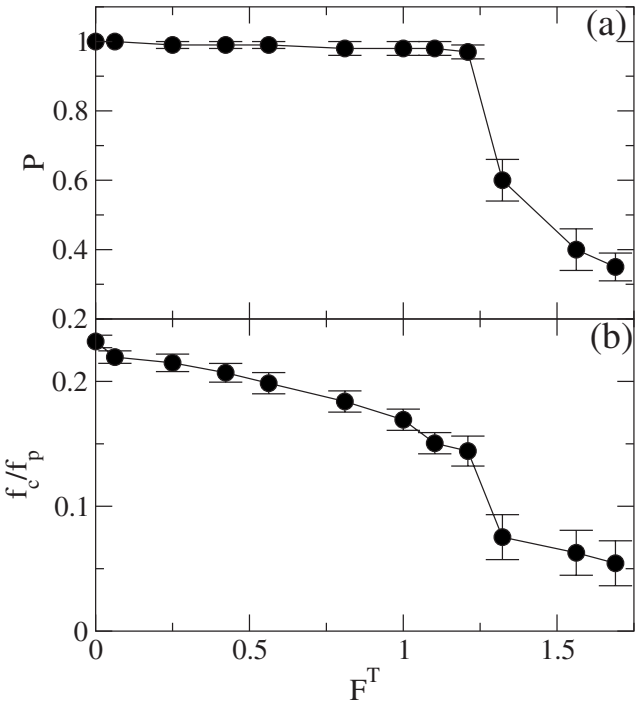

FIG. 13. (a) Fraction P of orientationally ordered dimers versus temperature F^T for the honeycomb pinning lattice in Figs. 5(a) and 5(b) with $f_p=0.5f_0$ and $B/B_\phi^H=2.0$. (b) The depinning force f_c/f_p vs F^T for the same sample.

Figure 13(b) shows the depinning force f_c/f_p as a function of F^T for the honeycomb pinning lattice at $B/B_\phi^H=2$ from Fig. 13(a). The orientationally ordered dimer state has a well defined depinning threshold which decreases monotonically with increasing F^T. Once the dimer orientational order is lost, f_c/f_p undergoes a corresponding pronounced drop. This is consistent with the results presented earlier in which vortex states that lack orientational order have a significantly lower value of f_c/f_p than orientationally ordered states. We note that in the experimental studies on honeycomb arrays of Ref. 33, as the temperature was increased, the matching effects at $B/B_\phi^H=3.5$ and 4.5 were lost while the matching effects at $B/B_\phi^H=1$ and 2 persisted. This is consistent with our finding that a significant drop in the strength of the matching effect appears at the melting of the vortex molecular crystals, which we expect to be present at $B/B_\phi^H=3.5$ and 4.5.

VI. VORTEX MOLECULAR CRYSTAL PHASE DIAGRAM

A. Honeycomb dimer state at $B/B_\phi^H=2$

By conducting a series of simulations and measuring P and the diffusion D, we determine the phase diagram of the different phases for the $B/B_\phi^H=2.0$ dimer state of the honeycomb pinning array. The diffusion is given by

$$D=\left\langle\frac{|\mathbf{R}_i(t+dt)-\mathbf{R}_i(t)|}{dt}\right\rangle, \tag{4}$$

with $dt=1000$ simulation time steps. The resulting phase diagram as a function of temperature F^T and pinning strength f_p is given in Fig. 14. The behavior of the sample at $f_p=0.5f_0$ was shown in Figs. 12 and 13 where a vortex molecular crystal forms for $0\leqslant F^T<1.25$, a vortex plastic crystal is present for $1.25\leqslant F^T<2.3$, and at $F^T\geqslant 2.3$ the dimer states break apart and the vortices diffuse throughout the sample in a modulated liquid state induced by the substrate. Figure 14 indicates that there is no vortex plastic crystal phase for $f_p<0.35f_0$ but that the vortex molecular crystal melts directly to the modulated vortex liquid for $0.15f_0<f_p<0.35f_0$.

For $f_p\leqslant 0.15f_0$, the pinning force is not strong enough to overcome the elastic energy of the vortex lattice and the low temperature ground state is not the dimer state shown in Figs. 5(a) and 5(b) but a partially pinned triangular vortex

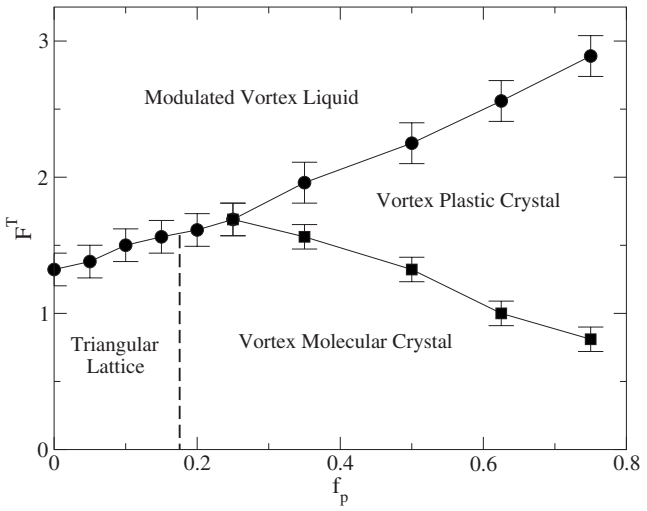

FIG. 14. The temperature F^T vs pinning strength f_p phase diagram for the honeycomb pinning array at $B/B_\phi^H=2.0$ in the dimer state. The four phases include the vortex molecular crystal phase illustrated in Figs. 5(a) and 5(b), a vortex plastic crystal phase shown in Figs. 13(a) and 13(b), a modulated vortex liquid phase where motion occurs throughout the sample, and a partially pinned triangular vortex lattice that forms at low f_p and low temperature which is described in Fig. 15. Circles: onset of significant diffusion as determined from the diffusion measurement D. Squares: loss of orientational order as determined from P, the fraction of orientationally ordered dimers.

lattice. This state is illustrated in Figs. 15(a) and 15(b) at $f_p=0.15f_0$ and $F^T=0$. The triangular vortex lattice still shows a partial commensuration effect with the substrate and is aligned in such a way that half of the pinning sites are occupied by a vortex. The unpinned vortices form a kagomé structure oriented 30° from the original triangular lattice, where here the pinned vortices take the place of the missing pinning sites in the kagomé lattice.

The melting temperature in Fig. 14 from the partially pinned triangular lattice to the modulated vortex liquid increases with increasing f_p. The existence of pinned vortices in the triangular vortex lattice effectively stiffens the lattice, and this effect becomes more pronounced as f_p increases. The transition temperature from the vortex plastic crystal state to the modulated vortex liquid also increases with increasing f_p since a higher temperature is required to enable the vortices to escape from the stronger pinning sites.

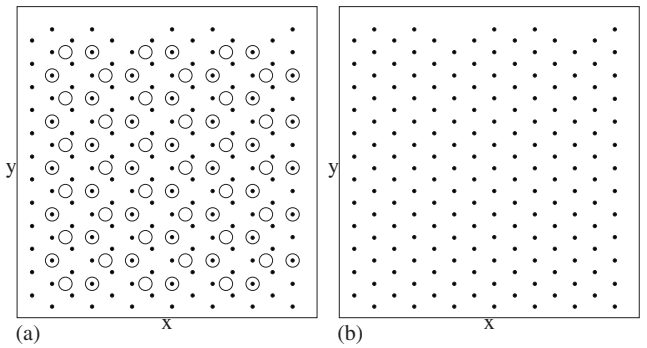

FIG. 15. (a) Vortex positions (black dots) and pinning site locations (open circles) in a portion of the sample for the honeycomb pinning array in Fig. 14 at $B/B_\phi^H=2.0$ and $f_p=0.15f_0$ in the partially pinned triangular lattice phase at $F^T=0$. (b) Vortex positions only.

An interesting feature in the phase diagram of Fig. 14 is the fact that the transition temperature between the vortex molecular crystal and vortex plastic crystal states *decreases* with increasing f_p. The same trend was observed for colloidal molecular crystals as a function of temperature versus substrate strength.[25,27,28] In the colloidal case, each dimer is trapped in a substrate minima, and as the substrate strength increases, the distance between the two colloids in each dimer decreases. As a result, the strength of the effective quadrupole interaction between the dimers decreases, lowering the transition temperature. For the case considered here, the vortex dimers in the honeycomb pinning lattice do not sit in the pinning sites and are not directly affected by the increase of f_p. The dimers do, however, interact with the vortices which are trapped by the pinning sites, and these pinned vortices become less mobile and less able to fluctuate as f_p increases. At low f_p, the pinned vortices that are closest to the ends of each dimer move to the outer edges of the pinning sites in order to sit as far as possible from that dimer. This produces a flatter interstitial confining potential along the length of the dimer in the center of the honeycomb plaquette and permits the interstitial vortices that form the dimers to move further away from each other. For higher f_p, the pinned vortices are shifted toward the center of the pinning sites and closer to the dimer. This produces a stronger confining force on the interstitial dimer and brings the vortices that form the dimer closer together, reducing the effective quadrupole interaction between neighboring dimers and lowering the transition temperature between the vortex molecular crystal and vortex plastic crystal states. This transition line is likely to saturate at very high f_p when the pinned vortices are constrained to sit at the very center of the pinning sites and cannot adjust their positions in response to the orientation of the neighboring dimers. We note that it is possible that for very high values of f_p, a new interstitial liquid phase could form in which the dimers break apart and the interstitial vortices hop from one interstitial region to another while the vortices in the pinning sites remain immobile.

It is beyond the scope of this work to determine the exact nature of the transitions in the phase diagram of Fig. 14; however, since the overall system appears to be very similar to the colloidal case, we can argue from the results for the colloidal system that the vortex molecular crystal to vortex plastic crystal transition is probably Ising-like. The vortex plastic crystal to modulated vortex liquid state transition is mostly likely an activated crossover.

B. Honeycomb trimer state at $B/B_\phi^H=2.5$

In order to determine how general the features of the phase diagram in Fig. 14 are, we consider the case of the honeycomb lattice at a field of $B/B_\phi^H=2.5$ where an ordered arrangement of trimers occurs, as seen in Figs. 5(c) and 5(d). We find the same general melting behavior as for the dimers.

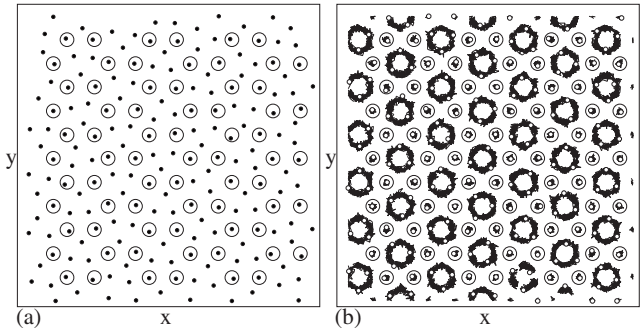

FIG. 16. (a) The vortex positions (black dots) and pinning site locations (open circles) in a portion of the sample for the honeycomb pinning array in Figs. 5(c) and 5(d) with $f_p=0.5f_0$ and $B/B_\phi^H=2.5$ at a temperature of $F^T=1.1$. (b) The same as in (a) with vortices (white dots), pinning sites (open circles), and vortex trajectories (black lines) over a fixed time period of 10^3 simulation time steps.

In Fig. 16(a), we illustrate the vortex plastic crystal at $F^T=1.1$. Here, each pinning site captures one vortex and the interstitial trimers do not have orientational ordering. In Fig. 16(b), the vortex trajectories indicate that the trimers are rotating in a manner similar to the dimers in Fig. 12. For higher temperature F^T, the trimers break apart and we observe diffusion throughout the entire sample.

By conducting a series of simulations for varied temperature F^T and pinning strength f_p and measuring the fraction of aligned trimers and the diffusion, we map out the phase diagram for the trimer state at $B/B_\phi^H=2.5$, as shown in Fig. 17. The general features of the phase diagram at $B/B_\phi^H=2.5$ are similar to the phase diagram at $B/B_\phi^H=2.0$ in Fig. 14; however, there are some noticeable differences. For a given pinning strength, the trimers disorder at a significantly lower temperature than the dimers. For example, at $f_p=0.5f_0$, the trimers lose orientational order at $F^T=0.5$, while for dimers the orientational order persists up to $F^T=1.25$. This reflects the fact that the effective multipole interaction between trimers is weaker than the effective quadrupole interaction between dimers. We also note that at $F^T=0.0$, we observe a peak in f_c/f_p at $B/B_\phi^H=2.5$, shown in Fig. 2, while the experiments of Ref. 33 did not find a peak at this filling. This could be due to the fact that the trimer melting temperature is relatively low, and the experiments may have been performed above the trimer melting temperature.

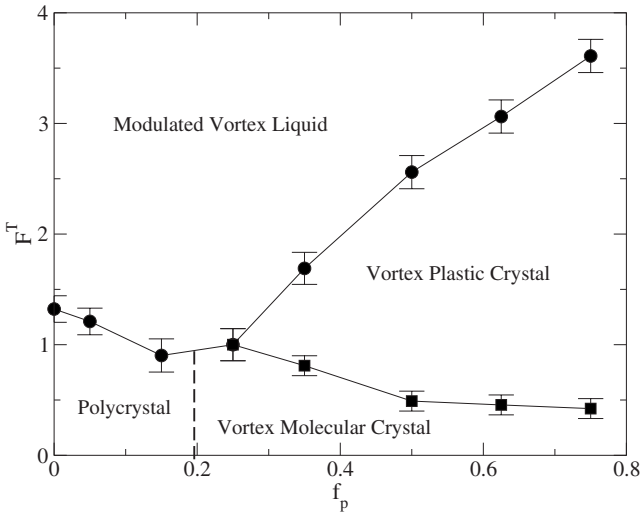

FIG. 17. The temperature F^T vs pinning strength f_p phase diagram for the honeycomb pinning array at $B/B_\phi^H=2.5$ in the trimer state. The vortex molecular crystal phase is illustrated in Figs. 5(c) and 5(d). The vortex plastic crystal phase is shown in Fig. 16. In the modulated vortex liquid, there is diffusion throughout the entire sample, while at low f_p and F^T a partially pinned polycrystalline triangular lattice forms which is described in Fig. 18. Circles: onset of significant diffusion. Squares: loss of trimer orientational order.

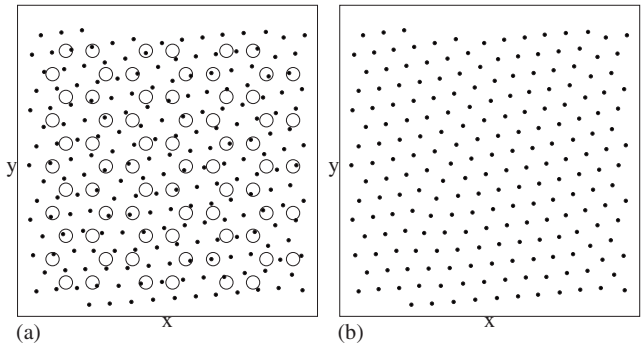

FIG. 18. (a) Vortex positions (black dots) and pinning site locations (open circles) in a portion of the sample for the honeycomb pinning array in Fig. 17 at $B/B_\phi^H=2.5$ and $f_p=0.1f_0$ in the polycrystalline vortex state at $F^T=0$. (b) Vortex positions only.

For $f_p<0.2f_0$ and low temperatures, the ordered trimer state is lost and the vortices form a partially ordered triangular lattice, as shown in Fig. 18. At $B/B_\phi^H=2.5$, the vortices are unable to simultaneously sit in a triangular lattice and align with the pinning sites, as in the partially pinned triangular lattice of Fig. 15 at $B/B_\phi^H=2.0$. Instead, we find a polycrystalline state composed of a triangular lattice that contains dislocations and grain boundaries. The melting line between the polycrystalline state and the modulated vortex liquid in Fig. 17 at $B/B_\phi^H=2.5$ decreases in temperature with increasing f_p. This is the opposite of the behavior of the melting line between the partially pinned triangular lattice and the modulated vortex liquid at $B/B_\phi^H=2.0$ shown in Fig. 14 and occurs because the increasing f_p leads to an increase of the polydispersity in the lattice, depressing the melting temperature. At $f_p=0.0$ and $B/B_\phi^H=2.5$, a dislocation-free triangular lattice forms, which has a higher melting temperature than the defected lattice that appears at finite pinning strength.

We have also studied the effect of temperature on the orientational ordering of the n-mer states for $B/B_\phi^H\geqslant 3$ in the honeycomb lattice at fixed $f_p=0.5$ (not shown). In general, we find that at fields with no long-range orientational order, such as $B/B_\phi^H=3$, the n-mers undergo thermally induced rotations at any finite temperature so there is only a vortex plastic crystal phase which melts to the modulated vortex liquid. At the other orientationally ordered fillings, we observe a finite temperature transition from an ordered vortex molecular crystal state to a vortex plastic crystal state.

We have performed finite temperature simulations for the kagomé system as well and find the same general results (not

shown) as in the honeycomb system. At orientationally ordered fillings, there is a low temperature ordered vortex molecular crystal state which melts into an intermediate vortex plastic crystal state. Additionally, the orientationally disordered states at $B/B_\phi^K=8/3$ and 11/3 show only vortex plastic crystal and vortex modulated liquid phases at finite temperature.

Our results agree with the previous study of thermal motion of vortices on kagomé pinning arrays. In Ref. 31, at the second matching field $B/B_\phi=2$, which corresponds to our $B/B_\phi^K=8/3$, the interstitial vortex triangles did not form an orientationally ordered state but instead created what was termed a kagomé state at finite temperatures. This kagomé state corresponds to our general class of vortex plastic crystals in which the n-mers are orientationally disordered. We note that at $B/B_\phi^K=8/3$, we observe no large peak in f_c/f_p, as shown in Fig. 7, and the interstitial vortex trimers have no long-range orientational order, as seen in Fig. 10(a). In contrast, at $B/B_\phi^K=7/3$, we find an orientationally ordered vortex molecular crystal state in which all of the trimers are aligned, shown in Fig. 9(e), which has a finite temperature transition to a vortex plastic crystal.

The vortex plastic crystals have similarities to the recently proposed vortex Peierls states for vortices in a Bose-Einstein condensate interacting with a corotating periodic optical lattice.[23] The optical lattice structure is, in fact, a kagomé array; however, in Ref. 23, there is an additional potential minima imposed on the center of the kagomé plaquettes. The vortex trimer state which forms at a filling of 1/3 on the dual dice lattice tunnels between the two degenerate configurations. This state is very similar to the vortex trimer state we observe in which the trimers are undergoing thermally induced rotations, as shown in Fig. 16.

VII. EFFECT OF PINNING STRENGTH

The strength f_p of the pinning sites determines whether it is possible for a vortex molecular crystal state to form. In Sec. VI, we showed that in the honeycomb pinning lattice at $B/B_\phi^H=2.0$, low f_p, and low temperature, the partially pinned triangular vortex lattice illustrated in Fig. 15 appears instead of the vortex dimer molecular crystal shown in Fig. 5(a). This results when the elastic energy of the vortex lattice, which favors a triangular vortex configuration, overcomes the energy of the pinning sites. Similarly, at $B/B_\phi^H=2.5$, the partially pinned polycrystalline vortex lattice seen in Fig. 18 forms instead of a vortex trimer molecular crystal at low f_p. In general, partially pinned phases will not occur in superconductors with arrays of holes because the pinning is too strong but may form for the weaker pinning found for vortices in superconductors with blind hole arrays or for colloids on optical trap arrays. Previous work has shown that a competition between the symmetry of the pinning lattice and a triangular lattice of interacting particles can lead to structural transitions of the particle lattice. Transitions from square to partially pinned vortex lattices have been observed in vortex simulations,[21,37] while partially pinned phases have recently been demonstrated experimentally for macroscopic Wigner crystals in square pinning arrays.[30] As the pinning strength is reduced at the first matching filling, Ref. 30 shows that a transition occurs from a square Wigner lattice where each pinning site captures one charge to a partially pinned triangular lattice. A similar transition appears at the second matching filling. If the substrate had been triangular, then at the first matching filling there would have been no structural transition of the charge lattice since its symmetry would coincide with that of the pinning lattice. At the second matching filling on a triangular array, the particles form a honeycomb lattice when the pinning is strong,[7] but as the pinning strength is weakened, a transition to a partially pinned phase should occur that allows the particle lattice to have a more triangular ordering. For vortices in honeycomb and kagomé pinning arrays, we expect a transition from a completely pinned phase to a partially pinned phase to occur as a function of pinning strength even at the first matching field.

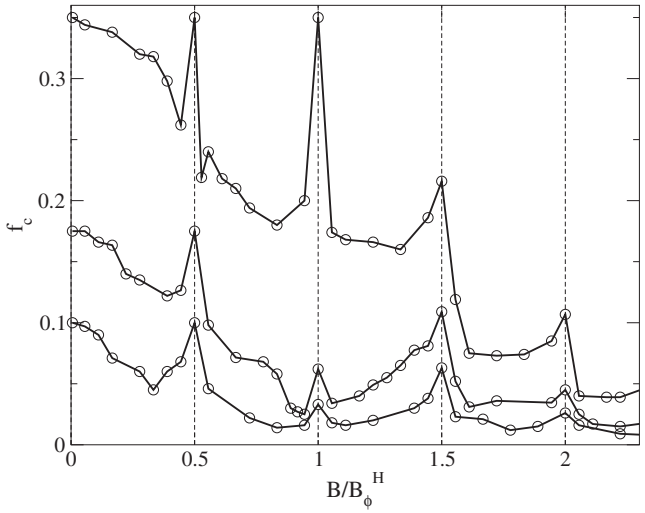

FIG. 19. f_c vs B/B_ϕ^H for the honeycomb pinning array from Fig. 2 with $f_p=0.35f_0$, $0.175f_0$, and $0.1f_0$, from top to bottom. The results for $f_p=0.5f_0$ appear in Fig. 2.

Since there are a rather large number of possible different vortex configurations shown in Secs. III and IV, we focus here on three cases which indicate the general behavior for both the honeycomb and kagomé arrays at the different matching fields as the pinning strength is varied. In Fig. 19, we plot f_c vs B/B_ϕ^H at pinning strengths of $f_p=0.1f_0$, $0.175f_0$, and $0.35f_0$ for the honeycomb pinning array from Fig. 2, which contains the results at $f_p=0.5f_0$. The vortex configurations at $f_p=0.35f_0$ are the same as those at $f_p=0.5f_0$ described in Sec. III, and the depinning force f_c at $B/B_\phi^H=1/2$ and 1.0 is higher than f_c at $B/B_\phi^H=1.5$ and 2.0. As f_p is reduced below $0.35f_0$, the overall f_c at all the fields decreases, but not uniformly, as f_c at $B/B_\phi^H=1.0$ drops below the value of f_c at $B/B_\phi^H=0.5$ and 1.5. This crossover in f_c with decreasing pinning force results when the vortex lattice at $B/B_\phi^H=1$ undergoes a transition from a fully pinned honeycomb lattice such as that illustrated in Figs. 4(c) and 4(d) to the partially pinned distorted square lattice shown in Figs. 20(a) and 20(b) at $f_p=0.175f_0$. Here, although there are an equal number of pins and vortices, half of the pinning sites are occupied while the other half are empty, resulting in a

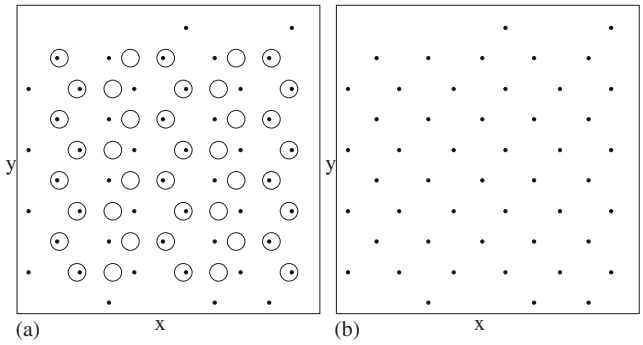

FIG. 20. (a) The vortex positions (black dots) and pinning site locations (open circles) in a portion of the sample for the honeycomb pinning array in Fig. 19 at $B/B_\phi^H=1.0$ and $f_p=0.175f_0$ where a distorted square vortex lattice forms. (b) Vortex positions only. For higher f_p, all the vortices are located at pinning sites and the state shown in Figs. 4(c) and 4(d) occurs.

significant decrease of the depinning threshold. The elastic energy of the distorted square vortex lattice at $f_p \leqslant 0.35f_0$ is lower than the honeycomb vortex lattice that forms at higher f_p.

In Fig. 21(a), we plot f_c vs f_p for the honeycomb array at $B/B_\phi^H=1/2$, 1.0, and 1.5. At $B/B_\phi^H=1/2$, the triangular vortex lattice illustrated in Figs. 4(a) and 4(b) forms. There is no transition to a partially pinned state as f_p decreases at this field since there is no competition between the vortex lattice symmetry and the pinning symmetry. All the vortices remain trapped at pinning sites for arbitrarily low f_p. Since the vortex lattice is completely symmetrical, the depinning force f_c is directly proportional to f_p, as shown in Fig. 21(a). At $B/B_\phi^H=1.0$, all the vortices are pinned at the pinning sites in a honeycomb lattice for $f_p>0.35f_0$ and f_c increases linearly with f_p. For $f_p \leqslant 0.35f_0$, the system enters the partially pinned phase illustrated in Fig. 20. At the same time, f_c drops abruptly to a lower value and then decreases more slowly with decreasing f_p. The vortex lattice is always triangular at $B/B_\phi^H=1.5$, as seen in Figs. 4(e) and 4(f), and there is no sharp change in f_c vs f_p since there is no structural transition in the vortex lattice when f_p is varied. For $f_p<0.35$, f_c is higher at $B/B_\phi^H=1.5$ than at $B/B_\phi^H=1.0$, as also indicated in Fig. 19. The depinning force at $B/B_\phi^H=1.5$ increases more slowly than linearly with f_p, which is more clearly seen in Fig. 21(b) where the range of f_p is extended to $2.0f_0$. Here, the depinning force is determined by the 1/3 of the vortices which are not confined at pinning sites. As f_p increases, the vortices at the pinning sites are more strongly pinned; however, the caging potential which pins the interstitial vortices saturates.

At $B/B_\phi^H=2.0$, we have already shown in Sec. VI B that a transition to the partially pinned state illustrated in Fig. 15 occurs as f_p decreases. As a result, there is a jump in f_c near $f_p=0.35f_0$ (not shown) similar to what we find for $B/B_\phi^H=1$ in Fig. 21(a). For high f_p, the f_c versus f_p curve for $B/B_\phi^H=2$ resembles that at $B/B_\phi^H=1.5$ shown in Fig. 21(b), with a saturation in the depinning force for the interstitial vortex dimers. We thus expect two dominant behaviors of f_c versus f_p at higher matching fields. For those fields where the overall vortex lattice is triangular, such as $B/B_\phi^H=1.5$ and 4.5 in the honeycomb pinning array [Figs. 4(e) and 4(f) and Figs. 6(e) and 6(f), respectively] as well as $B/B_\phi^K=4/3$, 4, and 16/3 in the kagomé array [Figs. 8(e) and 8(f) and Figs. 11(e) and 11(f), respectively], f_c saturates at high values of f_p but has no transition at low values of f_p. For the matching fields with nontriangular vortex configurations, a transition to a more triangular state at low f_p occurs which is accompanied by a drop in f_c, and in addition there is a saturation of f_c at high f_p which always occurs in the presence of interstitial vortices. It is also possible that there could be more than one structural transition as f_p decreases. For example, we have shown a transition from a honeycomb vortex lattice to a distorted square lattice (Fig. 20) in the honeycomb pinning lattice at $B/B_\phi^H=1$. At extremely low f_p, a second transition to a completely triangular vortex lattice should occur.

VIII. DISCUSSION

In this work, we only considered the case where each pinning site could capture at most one vortex; however, other types of vortex phases and commensurability effects may occur in real samples if multiple vortices are captured by the pins. If the pinning is very strong, the first few matching fields would correspond to the presence of multiquanta vortices at the pinning sites and no interstitial vortices. The vortices would start to enter the interstitial regions only once the pinning site saturation field is reached. For kagomé and honeycomb lattices of this type, strong commensurability effects would appear at only the integer matching fields below the pinning saturation field and would cross over to matching effects at the $n/2$ or $n/3$ fields once the pinning saturation occurs. Alternatively, individually quantized vortices may form at low fields, while multiply quantized vortices may appear in the pinning sites only at high fields where the

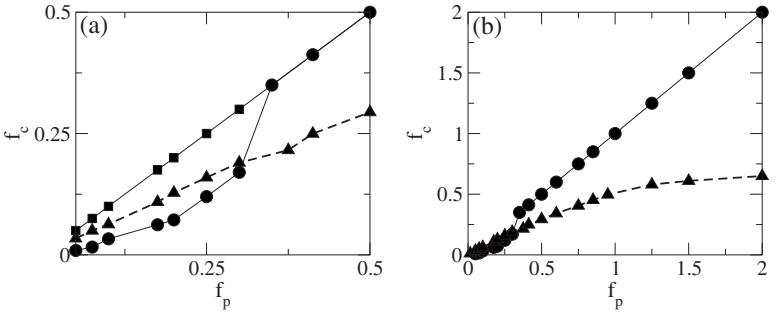

FIG. 21. (a) The depinning force f_c vs f_p for the honeycomb pinning array at $B/B_\phi^H=1/2$ (squares), $B/B_\phi^H=1.0$ (circles), and $B/B_\phi^H=1.5$ (triangles). At $f_p<0.35$, the vortex lattice at $B/B_\phi^H=1$ is a distorted square lattice rather than a honeycomb lattice, and therefore f_c for $B/B_\phi^H=1$ drops below f_c for $B/B_\phi^H=1/2$. (b) The same as in (a) for $B/B_\phi^H=1$ (circles) and $B/B_\phi^H=1.5$ (triangles) but extended to higher f_p, showing that there is a saturation in f_c for $B/B_\phi^H=1.5$.

vortex lattice constant is small. In such a case, noninteger matching effects would appear at low fields followed by a crossover to integer matching effects at higher fields. In Ref. 9, where continuum simulations of square pinning arrays were performed, it was proposed that multiple interstitial vortices can merge to form a single giant interstitial vortex. In the case of the honeycomb and kagomé arrays, singly quantized vortices could occupy the pinning sites while multiply quantized vortices sit in the large interstitial sites. In this scenario, the overall vortex lattice would be triangular and commensurability peaks would be observable at all fields $n/3$ or $n/2$. If multiple quantization of the interstitial vortices occurs, there would be no finite temperature phase transition from a vortex molecular crystal to a vortex plastic crystal and all of the matching peaks would vanish at the same rate with temperature. Additionally, since the vortex lattice symmetry would be triangular at every matching field, there would be no missing matching peaks due to the formation of vortex plastic crystals. These effects are not seen in the experiment of Ref. 33, suggesting that multiple quantization of vortices is not occurring.

As stated previously, many of the orientationally ordered n-mer states are related to various types of Ising and three-state Potts models. It may be possible to create honeycomb and kagomé pinning arrays that have an additional anisotropy in one direction. This would bias some of the degenerate directions of the n-mer states so that only certain directions of the n-mer ordering would occur. Also, highly frustrated states could be created such as incommensurate fillings composed of mixtures of two different n-mer species. Ordered colloidal molecular crystal alloy states formed by mixtures of different n-mers have been proposed in Ref. 38, and similar states may occur for the vortex system. It is likely that such mixtures would have extremely long relaxation times to reach the ordered ground state. These mixtures might produce glassy dynamics and have interesting time-dependent or history-dependent properties.

In addition to allowing the creation of vortex molecular crystal and vortex plastic crystal states, honeycomb and kagomé pinning arrays may also be valuable for the general enhancement of pinning. If pinning sites are placed in a honeycomb or kagomé arrangement, higher pinning can be achieved at matching fields above the first matching field compared to a triangular pinning array with an equal number of pinning sites. This is illustrated in Fig. 22, where f_c/f_p is plotted as a function of matching field for a triangular, kagomé, and honeycomb pinning arrays of equal pinning strength $f_p=0.5f_0$. Below the first matching field, there is little difference between the depinning force for the three arrays; however, above the first matching field, the honeycomb array shows a pronounced enhancement of f_c over the triangular array and the kagomé array also shows a smaller enhancement of f_c compared to the triangular array. This suggests that for different arrays with the same number of pinning sites, the honeycomb and kagomé pinning arrays have an overall higher critical current than triangular pinning arrays.

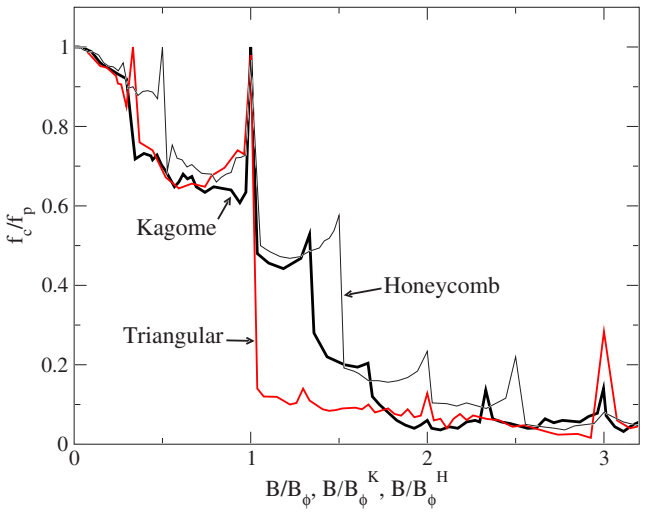

FIG. 22. (Color online) f_c/f_p versus B/B_ϕ for the triangular pinning array (red medium line), versus B/B_ϕ^K for the kagomé array (dark line), and versus B/B_ϕ^H for the honeycomb array (light line) at $f_p=0.5f_0$.

IX. CONCLUSION

We have used numerical simulations to study the vortex states in honeycomb and kagomé pinning arrays in the limit where only one vortex is captured at each pinning site. For the honeycomb arrays, we find pronounced matching effects in the form of peaks in the depinning force at most fields $B/B_\phi^H=n/2$, where $n>2$, while for kagomé arrays pronounced matching effects occur at most fields $B/B_\phi^K=n/3$, where $n>3$. This is in contrast to the purely triangular pinning arrays which have prominent matching effects only at $B/B_\phi=n$ or at fields below the first matching field. For the honeycomb pinning array, a variety of vortex molecular crystal states occur. Here, multiple interstitial vortices occupy the large interstitial regions of the honeycomb pinning lattice and form effective dimer, trimer, and higher order n-mer vortex states. The n-mers interact via an effective quadrupole or higher order pole moment which can lead to an overall n-mer orientational ordering. This type of n-mer ordering is similar to the recently studied colloidal molecular crystal states observed for repulsively interacting colloidal particles on periodic substrates. For the honeycomb array, at some of the matching fields the n-mers do not order and there is no prominent peak in the depinning force at these fields. Our results agree well with recent experiments on honeycomb pinning arrays where strong peaks are observed at $B/B_\phi^H=n/2$ fillings with missing or weak peaks for the fields at which we observe disordered n-mer configurations. For the kagomé pinning arrays, we observe similar dimer, trimer, and n-mer ordered states which form herringbone or other ferromagneticlike configurations. Most of the missing commensuration peaks in the $B/B_\phi^K=n/3$ sequence correspond to the lack of n-mer ordering at zero temperature. We term the orientationally ordered vortex n-mer states "vortex molecular crystals." At finite temperature, we demonstrate the existence of a transition from an orientationally ordered vortex molecular crystal state to a state where the n-mers are rotating and lose their relative orientational ordering. We refer to this disordered state as a vortex plastic crystal. At higher temperatures, there is a crossover to a modulated vortex liquid

state where there is diffusion throughout the entire system. When the pinning strength is weak, we find that the vortex molecular crystal phases undergo a transition to partially pinned phases where the vortex lattice has triangular or partially triangular ordering and only a portion of the pinning sites are occupied. These results suggest that the vortex molecular crystal states have many similarities to the recently studied colloidal molecular crystal states and that the vortex molecular crystal to vortex plastic crystal transitions can be mapped to various types of spin systems such as Ising and Potts models.

ACKNOWLEDGMENTS

We thank M. Hastings for useful discussions. This work was carried out under the auspices of the National Nuclear Security Administration of the U.S. Department of Energy at Los Alamos National Laboratory under Contract No. DE-AC52-06NA25396.

[1] A. T. Fiory, A. F. Hebard, and S. Somekh, Appl. Phys. Lett. **32**, 73 (1978).
[2] V. V. Metlushko, M. Baert, R. Jonckheere, V. V. Moshchalkov, and Y. Bruynseraede, Solid State Commun. **91**, 331 (1994); M. Baert, V. V. Metlushko, R. Jonckheere, V. V. Moshchalkov, and Y. Bruynseraede, Phys. Rev. Lett. **74**, 3269 (1995).
[3] M. Baert, V. V. Metlushko, R. Jonckheere, V. V. Moshchalkov, and Y. Bruynseraede, Europhys. Lett. **29**, 157 (1995).
[4] K. Harada, O. Kamimura, H. Kasai, T. Matsuda, A. Tonomura, and V. V. Moshchalkov, Science **274**, 1167 (1996).
[5] S. B. Field, S. S. James, J. Barentine, V. Metlushko, G. Crabtree, H. Shtrikman, B. Ilic, and S. R. J. Brueck, Phys. Rev. Lett. **88**, 067003 (2002).
[6] V. Metlushko, U. Welp, G. W. Crabtree, Z. Zhang, S. R. J. Brueck, B. Watkins, L. E. DeLong, B. Ilic, K. Chung, and P. J. Hesketh, Phys. Rev. B **59**, 603 (1999); U. Welp, X. L. Xiao, V. Novosad, and V. K. Vlasko-Vlasov, *ibid.* **71**, 014505 (2005).
[7] C. Reichhardt, C. J. Olson, and F. Nori, Phys. Rev. B **57**, 7937 (1998).
[8] C. Reichhardt and N. Grønbech-Jensen, Phys. Rev. B **63**, 054510 (2001).
[9] G. R. Berdiyorov, M. V. Milosevic, and F. M. Peeters, Phys. Rev. Lett. **96**, 207001 (2006); G. R. Berdiyorov, M. V. Milosevic, and F. M. Peeters, Phys. Rev. B **74**, 174512 (2006).
[10] A. Bezryadin, Y. N. Ovchinnikov, and B. Pannetier, Phys. Rev. B **53**, 8553 (1996).
[11] S. Raedts, A. V. Silhanek, M. J. Van Bael, and V. V. Moshchalkov, Phys. Rev. B **70**, 024509 (2004).
[12] J. I. Martín, M. Vélez, J. Nogués, and I. K. Schuller, Phys. Rev. Lett. **79**, 1929 (1997).
[13] D. J. Morgan and J. B. Ketterson, Phys. Rev. Lett. **80**, 3614 (1998).
[14] M. J. Van Bael, J. Bekaert, K. Temst, L. Van Look, V. V. Moshchalkov, Y. Bruynseraede, G. D. Howells, A. N. Grigorenko, S. J. Bending, and G. Borghs, Phys. Rev. Lett. **86**, 155 (2001).
[15] J. I. Martín, M. Vélez, A. Hoffmann, I. K. Schuller, and J. L. Vicent, Phys. Rev. Lett. **83**, 1022 (1999).
[16] A. N. Grigorenko, S. J. Bending, M. J. Van Bael, M. Lange, V. V. Moshchalkov, H. Fangohr, and P. A. J. de Groot, Phys. Rev. Lett. **90**, 237001 (2003).
[17] D. J. Priour and H. A. Fertig, Phys. Rev. Lett. **93**, 057003 (2004).
[18] Q. H. Chen, G. Teniers, B. B. Jin, and V. V. Moshchalkov, Phys. Rev. B **73**, 014506 (2006).
[19] G. Karapetrov, J. Fedor, M. Iavarone, D. Rosenmann, and W.-K. Kwok, Phys. Rev. Lett. **95**, 167002 (2005).
[20] C. J. Olson Reichhardt, A. Libál, and C. Reichhardt, Phys. Rev. B **73**, 184519 (2006).
[21] C. Reichhardt and N. Grønbech-Jensen, Phys. Rev. Lett. **85**, 2372 (2000).
[22] H. Pu, L. O. Baksmaty, S. Yi, and N. P. Bigelow, Phys. Rev. Lett. **94**, 190401 (2005); J. W. Reijnders and R. A. Duine, Phys. Rev. A **71**, 063607 (2005).
[23] A. A. Burkov and E. Demler, Phys. Rev. Lett. **96**, 180406 (2006).
[24] S. Tung, V. Schweikhard, and E. A. Cornell, Phys. Rev. Lett. **97**, 240402 (2006).
[25] C. Reichhardt and C. J. Olson, Phys. Rev. Lett. **88**, 248301 (2002); M. Mikulis, C. J. Olson Reichhardt, C. Reichhardt, R. T. Scalettar, and G. T. Zimányi, J. Phys.: Condens. Matter **16**, 7909 (2004).
[26] M. Brunner and C. Bechinger, Phys. Rev. Lett. **88**, 248302 (2002).
[27] R. Agra, F. van Wijland, and E. Trizac, Phys. Rev. Lett. **93**, 018304 (2004).
[28] A. Sarlah, E. Frey, and T. Franosch, Phys. Rev. E **75**, 021402 (2007).
[29] K. Mangold, P. Leiderer, and C. Bechinger, Phys. Rev. Lett. **90**, 158302 (2003).
[30] G. Coupier, M. Saint Jean, and C. Guthmann, arXiv:cond-mat/0611582 (unpublished).
[31] M. F. Laguna, C. A. Balseiro, D. Domínguez, and F. Nori, Phys. Rev. B **64**, 104505 (2001).
[32] C. Reichhardt, C. J. Olson, R. T. Scalettar, and G. T. Zimányi, Phys. Rev. B **64**, 144509 (2001).
[33] T. C. Wu, J. C. Wang, L. Horng, J. C. Wu, and T. J. Yang, J. Appl. Phys. **97**, 10B102 (2005).
[34] M. Tinkham, *Introduction to Superconductivity* (Krieger, Malibar, FL, 1980).
[35] M. Schick, Surf. Sci. **125**, 94 (1983); E. J. Nicol, C. Kallin, and A. J. Berlinsky, Phys. Rev. B **38**, 556 (1988); S. E. Roosevelt and L. W. Bruch, *ibid.* **41**, 12236 (1990).
[36] T. J. Sluckin, J. Phys. A **21**, 1415 (1988); H. Vollmayr, Phys. Rev. B **46**, 733 (1992); H. Vollmayr and R. Kree, *ibid.* **47**, 14177 (1993).
[37] W. V. Pogosov, A. L. Rakhmanov, and V. V. Moshchalkov, Phys. Rev. B **67**, 014532 (2003).
[38] C. Reichhardt and C. J. Olson Reichhardt, Phys. Rev. E **71**, 062403 (2005).